Fretting wear behavior on LPBF processed AlSi10Mg alloy for different heat treatment conditions

Rashmi Saragur Nanjundaiah [a,b,**], Shrikantha Sasihithlu Rao [a], K. Praveenkumar [c], T Ram Prabhu [d], Arun Kumar Shettigar [a], Manjunath Patel G C [e], Emanoil Linul [f,*]

[a] Department of Mechanical Engineering, National Institute of Technology Karnataka, Surathkal, 575 025, Karnataka, India
[b] Department of Industrial and Production Engineering, The National Institute of Engineering, Mysore, 570 008, Karnataka, India
[c] Department of Materials Engineering, Indian Institute of Science, Bengaluru, 560 012, Karnataka, India
[d] Centre for Military Airworthiness and Certification, Defence Research and Development Organization, Bengaluru, 560 037, Karnataka, India
[e] Department of Mechanical Engineering, PES Institute of Technology and Management, Shivamogga, 577 204, Visvesvaraya Technological University, Belagavi, India
[f] Department of Mechanics and Strength of Materials, Politehnica University Timisoara, 1 Mihai Viteazu Avenue, Timisoara, 300 222, Romania

ARTICLE INFO

ABSTRACT

To widen the industrial application of additively manufactured (AM) parts, the study of fretting wear behavior is essential, as it ensures the safety and reliability that drive innovation in design and materials. This study explores the fretting wear behavior of the as-built and heat-treated state of AlSi10Mg alloy fabricated, viz., laser powder bed fusion (LPBF). Initially, the as-built and T5, T6, and stress-relieved (SR) heat-treated samples were examined using scanning electron microscopy (SEM) to gain insights into the microstructural changes. The as-built samples exhibited a higher hardness level (135 HV) primarily due to the presence of very fine microstructure of the α-Al cellular matrix with embedded Si. The α-Al cellular structure dissolved with various heat treatments, and Si particles coarsened. The hardness decreased to 85, 79, and 67 HV for the T5, T6, and SR conditions, respectively. Subsequently, fretting tests were conducted on the samples, applying various normal loads of 10, 50, and 100 N. Further, the samples were characterized by the coefficient of friction (COF), worn surface morphology, and wear volume loss. The investigation showed that the as-built material showed less wear volume loss under all loading conditions than the heat-treated conditions. Furthermore, the T5 heat treated sample had a lower wear volume when compared to the T6 and SR heat-treated samples. The heat-treated sample exhibits compressive stress, whereas the LPBF processed, the as-built sample shows tensile stress.

1. Introduction

Additive Manufacturing (AM) processes built parts layer by layer, based on three-dimensional (3D) data, due to their inherent layered construction method. The industry is currently benefiting from the ability to create intricate geometric structures and nearly net-shaped materials using a wide array of existing AM processes. These techniques hold the possibility to streamline design-to-manufacture timelines by consolidating numerous manufacturing steps into a single process. Specific AM methods provide the benefit of material efficiency, using only the required amount of material for the particular component being produced. The primary motivation for implementing AM is design freedom, allowing for the incorporation of features that are unattainable

through conventional methods, such as complex internal structures or channels [1], lattices [2], enabling light-weighting through topology optimization [3], and multi-material, and multifunctional devices [4]. In addition, it can integrate parts to form assemblies, thereby limiting the need for mechanical fixtures and post-processing steps. This also opens the door to cost-effective customized product manufacturing [5]. As AM's credibility continues to rise, its influence is anticipated to spread globally across businesses, where AM components are increasingly utilized in many industries [6,7].

Among the various AM techniques, LPBF is distinguished as a powerful AM technique, appropriate for working with a diverse range of metals, alloys, and metal matrix composites [8,9]. LPBF, also known as Selective Laser Melting (SLM), has increased adoption across industries due to its ability to create complex components directly from CAD

Nomenclature		HV	Hardness Vickers
		JCPDS	Joint Committee on Powder Diffraction Standards
3D	Three-dimension	LPBF	Laser Powder Bed Fusion
Al_2O_3	Aluminum Oxide	SEM	Scanning Electron Microscopy
μm	Micrometer	SLM	Selective Laser Melting
Al	Aluminum	SiC	Silicon Carbide
Al–Si	Aluminum–Silicon	SR	Stress Relieving
AM	Additive Manufacturing	T5	Direct Ageing heat treatment condition
COF	Coefficient of Friction	T6	Solution Treatment followed by Ageing heat treatment condition
EDS	Energy Dispersive Spectroscopy		
EOS	Electro Optical Systems	XRD	X-Ray Diffraction
HIP	Hot Isostatic Pressing	WEDM	Wire Electric Discharge Machining
HRC	Hardness Rockwell C scale		

models [10]. In LPBF, a high-power-density laser melts and fuses metal particles together. Since the inception of laser melting technology, considerable research has focused on the impacts of the rapid heating and cooling rates characteristic of SLM [9,11,12]. SLM is used more frequently to produce load-bearing parts, such as automobile power-trains, turbine components, and aerospace parts [13,14]. As the popularity of SLM grows, there is a growing emphasis on evaluating the mechanical performance of these parts to ensure their reliability and credibility.

On the other hand, processing aluminum (Al) alloys through SLM has posed challenges. Al powders are inherently lightweight have poor flow characteristics, high reflectivity, high thermal conductivity, low laser absorptivity, and susceptibility to oxidation. However, the successful application of SLM in processing aluminum alloys has primarily been achieved by casting alloys from the Aluminum–Silicon (Al–Si) group. Alloying aluminum with other metals helps overcome these initial challenges and enables effective processing via SLM. AlSi10Mg and AlSi12 alloys are the most commonly used aluminum alloys in SLM systems due to their excellent castability, low shrinkage, and significant Al–Si eutectic fraction [15]. AlSi10Mg, a hypo-eutectic alloy in the Al–Si family, is known for its excellent weldability, hardenability, and mechanical properties due to its proximity to the eutectic zone in the Al–Si phase diagram [16,17]. Adding Si to the alloy decreases its melting point, minimizes shrinkage, and improves fluidity. In Al–Si alloys, the minor Mg quantities enable heat treatment and enhance their mechanical properties, making them suitable for structural components [16–18].

Understanding the importance of post-production heat treatment for LPBF aluminum components has led to extensive research efforts [19–21]. These efforts are focused on creating innovative annealing methods to enhance these alloys mechanical properties and functional characteristics. This research branched into two distinct directions as follows [22]. The first trend involved adapting traditional thermal treatments, such as the T6 process, by modifying temperature and duration specifically for LPBF aluminum alloys. This adaptation aimed to optimize their properties. The second trend explored annealing treatments at various temperatures, conducting experiments to understand the phase transitions these treatments induced in the alloys. Subsequently, customized annealing methods and direct aging (T5) techniques have been established, specifically designed to align with the microstructural properties of LPBF Al–Si alloys. Stress relieving is also adopted along with T5 and T6 conditions. Tensile residual stresses are inevitable in additive manufacturing surfaces as during the layering process, the samples undergo rapid heating and sudden cooling, which results in tensile residual stress [23]. Stress relieving helps to minimize these residual stresses and enhances the mechanical properties.

Aboulkhair et al. [24] analyzed how T6 heat treatment affects the microstructure and mechanical properties of SLM-printed AlSi10Mg. The author disputes the common misconception about the hardenability

of SLM AlSi10Mg alloy through T6 heat treatment. The findings in this investigation demonstrated that the distinct starting microstructure led to softening rather than hardening. Also, the materials ductility was improved without substantially reducing strength. Wei et al. [25] confirmed that the Si/Mg2Si particle size increases when the solution-treated temperature rises and that T6 heat treatment significantly diminishes the sliding wear resistance of as-built samples.

Zhuo et al. [26] revealed that annealing or stress relief treatment at low temperatures (typically 300 °C for 2 h) reduces the internal residual stress. At the same time, lowering the stress relieving/annealing temperature can reduce microstructural coarsening [27,28]. Further, Giovagnoli et al. [29] stated that the alloy's equilibrium state (complete precipitation of Si from the Al primary phase) can be fully restored through low-temperature annealing. During this process, the Si network breaks down, forming Si particles, while the coarse grains (presence of Si particles in the primary α-Al) remain unaffected. These alterations in the microstructure contribute to a decrease in the static strength of the alloy, as evidenced by a reduction in hardness compared to its as-built condition [29].

Subramaniyan et al. [19] revealed that the micro-hardness of SLM-printed AlSi10Mg samples remained largely consistent between their as-printed and T5 heat-treated conditions. T6 heat-treated samples exhibited lower micro-hardness than both as-printed and T5 heat-treated samples. The as-printed samples' higher hardness values are likely due to rapid solidification and residual stresses.

Fiocchi et al. [22] point out that research on direct aging treatment, particularly T5, which involves annealing at lower temperatures for maximum hardness and strength enhancement through precipitation hardening, is less common than T6 or annealing. Two factors resulting from the T6 treatment experience are the primary drivers of interest in the T5 treatment of LPBFed Al–Si alloys. The spheroidization and coarsening of the eutectic Si phase are responsible for the sudden fall in strength that was previously observed [22,30]. Additionally, reports indicate that a solution treatment significantly reduces the supersaturation of alloying elements in the as-built Al matrix [31]. As a result, preceding the initial high-temperature solution treatment can maintain the original Si morphology and enable precipitation, capitalizing on matrix supersaturation from LPBF's rapid cooling.

Mechanical assemblies subjected to vibration may experience slight relative motion between their contacting surfaces, leading to fretting fatigue and fretting wear [32]. Fretting refers to the wear that happens when two solid surfaces in contact experience small amplitude oscillatory tangential movements relative to each other [33]. Fretting wear induces cracks and delamination in the surface during the process, which acts as a stress raiser and accelerates the fatigue failure [34]. The primary determinants within a contact situation encompass the material's physical attributes (such as hardness, yield strength, fracture toughness, and chemical inertness), the environmental factors (comprising temperature, relative humidity, and lubricants), as well as

the conditions of contact (including displacement stroke, vibration frequency, and contact pressure). Fretting is considered a characteristic of actual vibrating contacts due to the intricate interplay of multiple factors [34]. Recent research has focused on the SLM of AlSi10Mg, covering aspects such as process optimization [35–37], powder properties [38], surface roughness [39] crystallographic texture [17], hardness [40], microstructure and mechanical properties [40–44]. However, limited literature addresses the fretting wear behavior in SLM AlSi10Mg.

In LPBF, AM-printed parts exhibit inherent tensile stress at the surface, while compressive residual stresses are observed beneath the surface [45,46]. Compressive residual stresses are vital for enhanced service span life of industrial part applications (AM, aerospace, and automotive) by providing enough strength [47,48]. Compressive stress can enhance a material's fatigue life, increasing its durability and serving as a protective layer against tensile stresses that could cause cracking or other types of damage [49,50].

The present study aims to investigate the microstructural aspects of as-printed AlSi10Mg samples under various heat treatment conditions (T5, T6, and SR-stress relieved). These alloys are crucial for critical parts, and their low wear resistance can lead to catastrophic failures. To address this issue, the samples were subjected to fretting wear testing under various normal loads (10, 50, and 100 N) to gain insights into their fretting behavior.

2. Materials and methods

2.1. Material

The gas atomized AlSi10Mg powders having spherical morphology and typical composition of 10% of Si, 0.3% of Mg, and balance Al in wt. % with an average diameter ranging from 15 to 30 μm supplied by Electro Optical Systems (EOS) were used for printing the sample. The analysis of powder morphology was conducted using a Carl Zeiss FE-SEM 300. The particles exhibited predominantly spherical shapes, with some instances of satellite agglomeration, as illustrated in Fig. 1.

2.2. Laser powder bed fusion (LPBF)

The samples were built with LPBF using an EOSINT M 280 3D Printer equipped with 400 W Ytterbium fiber laser. Fig. 2 represents the schematic diagram of the LPBF process system. Samples were built to a cubical shape with $10 \times 10 \times 10$ mm^3 dimensions. The study selected specific optimum parameters based on pilot experiments and earlier investigations [51,52]. Before printing, the platform was heated to 30 °C. The AlSi10Mg was fabricated in an inert argon environment to
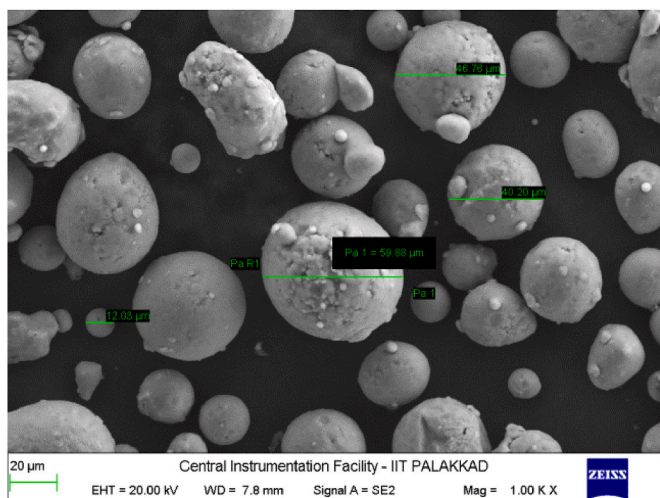

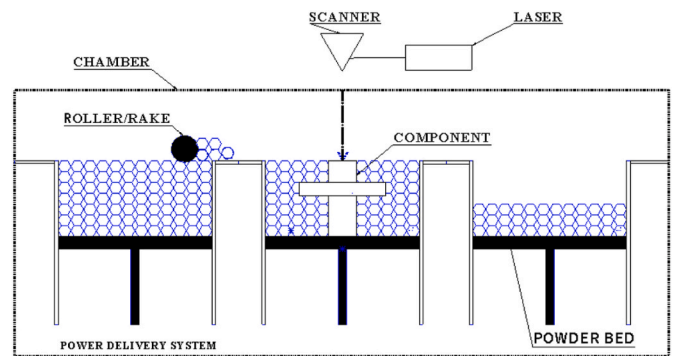**Fig. 1.** Morphology of AlSi10Mg powder.

Fig. 2. LPBF process system.

minimize oxygen's effect on the material properties.

Table 1 provides a summary of the optimized printing parameters. Furthermore, the components manufactured were detached from the substrate using Wire Electric Discharge Machining (WEDM). A comprehensive graphic representation of the different test processes carried out in the present work has been shown in Fig. 3.

2.3. Heat treatment

Based on earlier studies [51–56], the present investigation adopted the T5, T6, and SR heat treatment conditions after printing. The heat treatment was conducted using a box furnace (Make: Kemi muffle furnace, India). Direct Ageing was carried out at 170 °C for 3 h, and the furnace was cooled (T5). The solution treatment was performed at 540 °C for 2 h, with water quenching followed by artificial ageing at 170 °C for 3 h with subsequent furnace cooling (T6), and Stress Relieving was done at 320 °C for 3 h, with subsequent furnace cooling (SR). The T5, T6, and SR heat treatment curves are shown in Fig. 4.

2.4. Microstructure characterization

Post-printing, samples measuring $10 \times 10 \times 5$ mm^3 for microstructure analysis were taken from a plane perpendicular to the built direction. The surface of samples (as-printed and heat treated) at different conditions were polished sequentially using SiC abrasive papers with different granularities ranging from #100 to #2000 grit, followed by cloth polishing with diamond paste (0.25 μm) to obtain the final roughness of 0.4 μm. Keller's reagent (vol. 2.5% HNO$_3$, vol. 1% HF, vol. 1.5% HCl, vol. 95% H$_2$O) was used as an etchant to reveal the microstructure, which was characterized using a Scanning Electron Microscope (SEM) equipped with an Energy Dispersive Spectrometer (EDS).

2.5. X-ray diffraction (XRD)

X-Ray diffraction (XRD) measurements of As-printed and heat-treated samples were performed in a Malvern Panalytical's 3rd Gen Empyrean diffractometer equipped with Cu-Kα source (λ = 1.54 Å) within the range of 2θ from 10 to 110° at a scan rate of 5°/min. The obtained patterns were analyzed in the XpertHighscore V3 software to determine the development of the secondary phase's formation upon

Table 1
LPBF printing parameters.

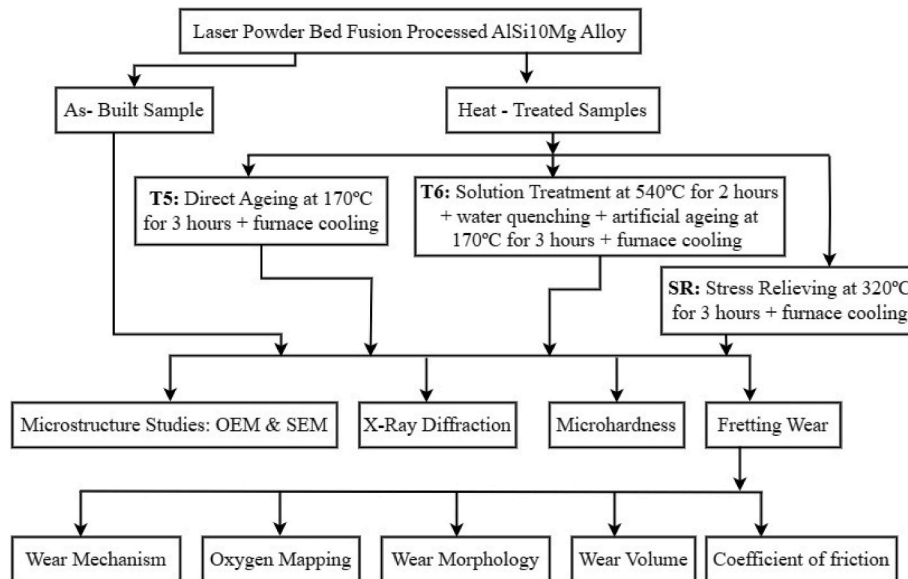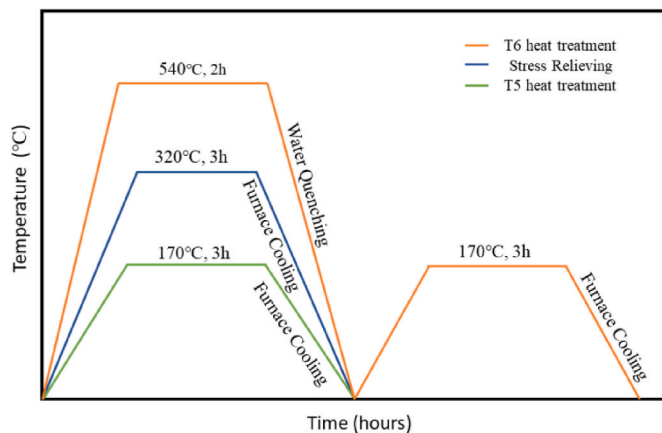| Parameters	Set Value
Laser power (W)	370
Scanning speed (mm/s)	1300
Scanning strategy	Rotating stripe (67°)
Inert gas	Ar
Built platform temp (°C)	30
Layer thickness (μm)	70

Fig. 3. Schematic diagram of the test process.

Fig. 4. Heat treatment curves (T5, T6 an SR).

heat treatment.

2.6. Residual stress measurement

Residual stress measurements were conducted using the standard XRD-based $\sin^2\psi$ method (PANalytical, Netherlands). The peaks utilized for analyzing the residual stress were {311}. The sample underwent tilting within the 40 to −40° range, totaling 33 steps. Cu-Kα radiation was used for the measurement, and the primary aperture size was 2 mm × 5 mm. Residual stress was measured on the build sample surface after polishing.

2.7. Microhardness

Vickers microhardness test of as-built samples and samples treated at different conditions were performed using Omni Tech microhardness tester by subjecting to a load of 100 g with a dwell time of 10 s. A minimum of ten indentations were considered on the mirror-polished flat surface, and the average values were reported.

2.8. Fretting wear

Fretting wear tests were conducted on as-printed and heat-treated

samples using a DUCOM fretting wear testing machine (Make: India), operated with WINDCOM 2010 software. Prior to the test, the samples were sequentially polished up to #2500 grit using SiC abrasive papers followed by velvet cloth polishing assisted with diamond aerosol spray to obtain a mirror finish. The test setup involved a ball-on-plate arrangement, where samples slide against a 6 mm diameter Alumina (Al_2O_3) ball with 55 HRC hardness under loads of 10, 50, and 100 N at a constant frequency and sliding amplitude of 15 Hz and 100 μm, respectively, for 10,000 cycles. The maximum Hertzian contact pressures were 974.9, 1667, and 2100 MPa, with corresponding maximum shear stress depths of 0.14, 0.054, and 0.069 mm for forces of 10, 50 and 100 N, respectively. Tests were conducted at 30 °C with a relative humidity range of 60% ± 5%. Three trials were conducted for each specimen, and the average was reported, with the standard deviation considered the error bar. The build directional surface was chosen for the fretting wear test. After the wear test, the sample was subjected to 3D-noncontact mode profilometry to analyze the wear volume loss. In addition, SEM analysis of worn surfaces explains the wear mechanism.

3. Results and discussion

3.1. Microstructure

Fig. 5(a–e) illustrates the as-built microstructure of AlSi10Mg, oriented parallel to the deposited layers (XY plane) and along the built direction (XZ plane). Fig. 5(a and b) illustrates the as-built microstructure, showcasing irregular geometries within the melt pool shape along the XY plane. These geometries intersect with previous layers at a 67° angle, as discussed in Section 2.2, depicting the layer orientation. From Fig. 5 (a), the dark spots represent the aluminum matrix, and dark spots indicate the silicon eutectic precipitates (Fig. 5 (b)). Irregularly sized macro pores are visible along the scan track boundary, while micropores are embedded within the scan matrix. The XY plane's top surface displays distinct scan track patterns, a common characteristic of LPBF-printed samples [57,58]. This microstructure reveals traces of the scanning laser as it melts the powder layer, forming small melt pools that quickly solidify. This rapid solidification results in directional growth features that deviate from equilibrium. Coarser grains are common along the melt pool border in layer-by-layer processes [59,60]. SEM analysis reveals a novel eutectic microstructure featuring exceptionally fine Si particles upon closer examination. The gray cellular features depict the primary α-Al matrix with a white, fibrous Si network [61].
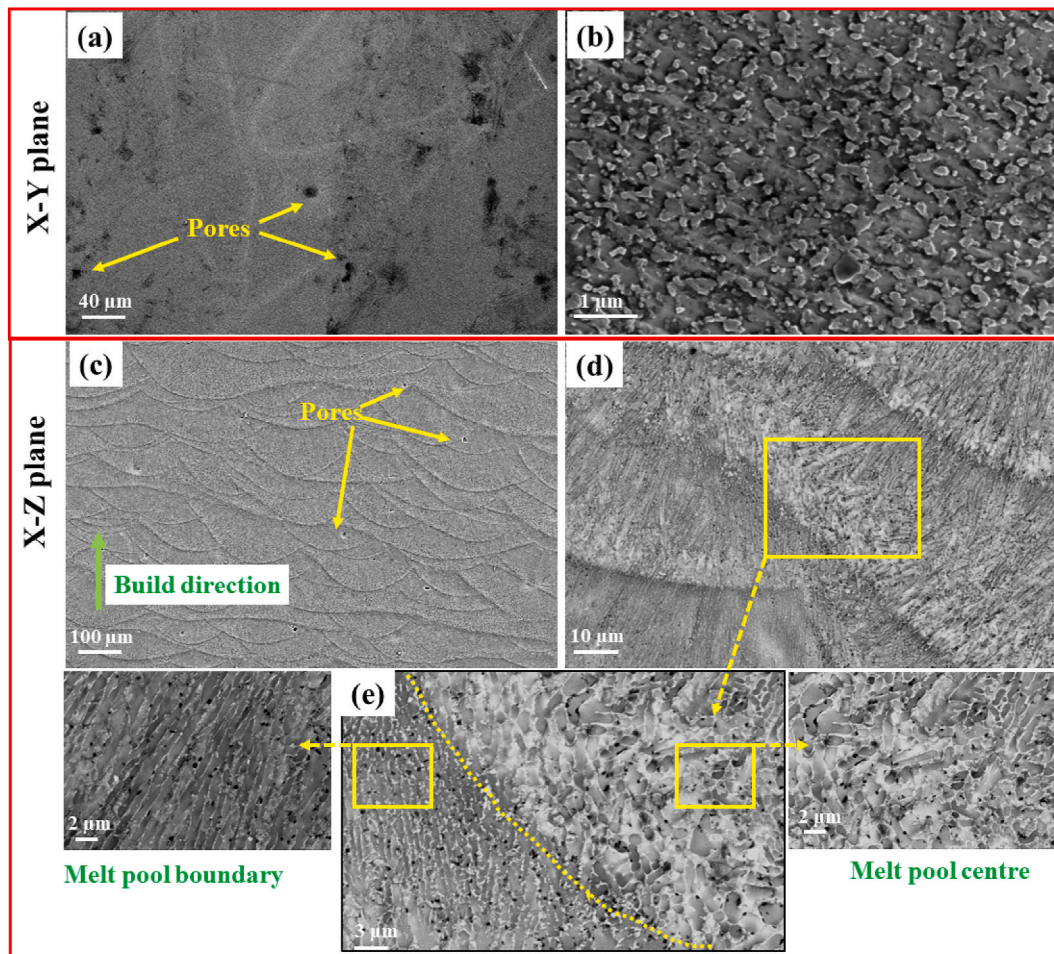
Fig. 5. SEM microstructure of as-built AlSi10Mg samples at (a–b) X–Y plane (surface) and (c–e) X-Z plane (along the built direction).

The X-Z direction shows the melt pools due to melting and re-solidification. There are two different microstructures observed. One is at the melt pool boundary and the melt pool center. The melt pool boundary shows a fine dendritic structure, and the center exhibits a cellular structure, as seen in Fig. 5 (e). The presence of precipitation of Si particles benefits the mechanical properties of the as-printed AlSi10Mg samples printed via LPBF. A similar observation was reported by Javidani et al. [62] and Delahaye et al. [61]. This cellular morphology influences the mechanical properties. Note that, no intermetallic compounds have formed, which suggests a substantial Si supersaturation in the Al matrix, a result of the rapid cooling during solidification. Fig. 6 shows that a higher concentration of Si is present in the cell boundaries, and also a limited amount of Mg particles is segregated into the matrix. A similar observation was noted by Zhou et al. [63].

Moreover, the microscopic examination of as-built samples revealed the presence of pores in both the X–Y and X-Z directions, attributed to the rapid cooling process [64,65]. These pores have a significant impact on the mechanical properties [66]. Consequently, researchers have been concentrating on mitigating these pores' presence through various post-processing techniques, such as Hot Isostatic Pressing (HIP). HIP has shown promise in effectively addressing internal pores; however, concerns arise regarding its ability to address surface-level pores and cracks [67,68]. Since properties like fatigue resistance, corrosion resistance, and resistance to fretting wear are heavily influenced by surface finish, HIP may not be the optimal solution for enhancing these specific properties.

Fig. 7 shows that T5 samples exhibit remarkably similar microstructures as those in as-built conditions in both X–Y and X-Z conditions.

Melt pools appears within the microstructure, retaining an ultrafine sub-micrometric composition of super-saturated α-Al cells surrounded by a eutectic Si network. Within the α-Al matrix cells and acicular Si precipitates were observed. The T5 treatment transforms the metastable as-built microstructure into a more stable state. This transformation is distinguished by the development of widespread Si particles and the partial reduction in melt pool presence (Fig. 7(d and e)). This condition also enhances the ductility by 64%, as reported by Rosenthal et al. [69]. In Fig. 8, Si particles are evident in the microstructure.

Fig. 9(a–e) displays the microscopic structure of a T6 heat-treated sample, aligned parallel to the layers deposited in the XY plane and also along the built direction in the XZ plane. Applying a T6 heat treatment result in a microstructure that unambiguously contrasts with the as-built state. To address the inherent anisotropy present in as-built samples, a T6 treatment is applied to achieve homogeneity [58]. Upon solution heat treatment (T6), the melt tracks completely disappear. This transformation occurs through two interdependent mechanisms. First, silicon atoms precipitate along pre-existing cellular boundaries after dissolving in the super-saturated as-built matrix. This precipitation process leads to the cellular boundaries becoming less distinct. Subsequently, Si branches undergo fragmentation and spheroidization. The reduction in silicon density is due to particle coalescence and Ostwald ripening process. In this phenomenon, larger particles increase in size at the cost of the smaller ones. Smaller particles, which possess higher surface energy and are less thermodynamically stable, are more susceptible to dissolution. As a result, motivated by the decrease in surface energy, the larger metastable precipitates undergo coarsening, essentially growing at the cost of the smaller ones. Heat treatment of the solid
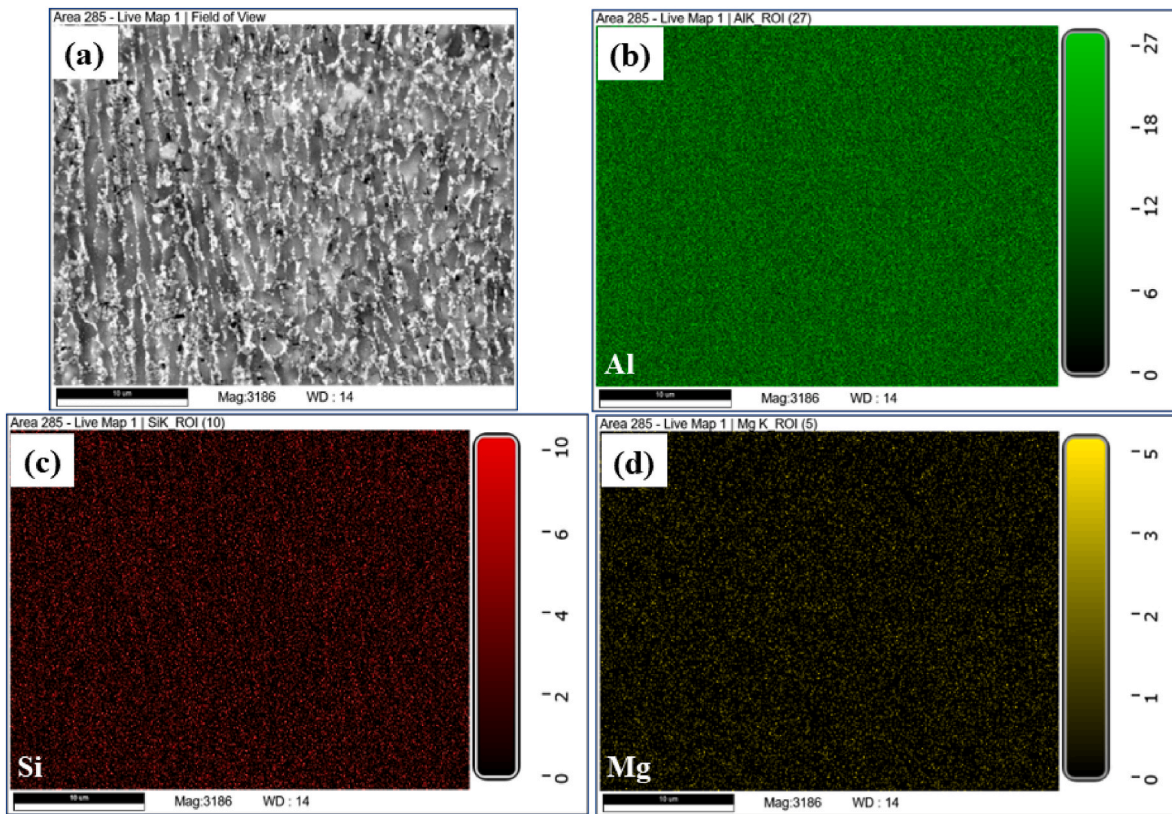
Fig. 6. Microstructure of X-Z plane (a) and elemental mapping of Al (b), Si (c) and Mg (d) for as-builtAlSi10Mg sample.
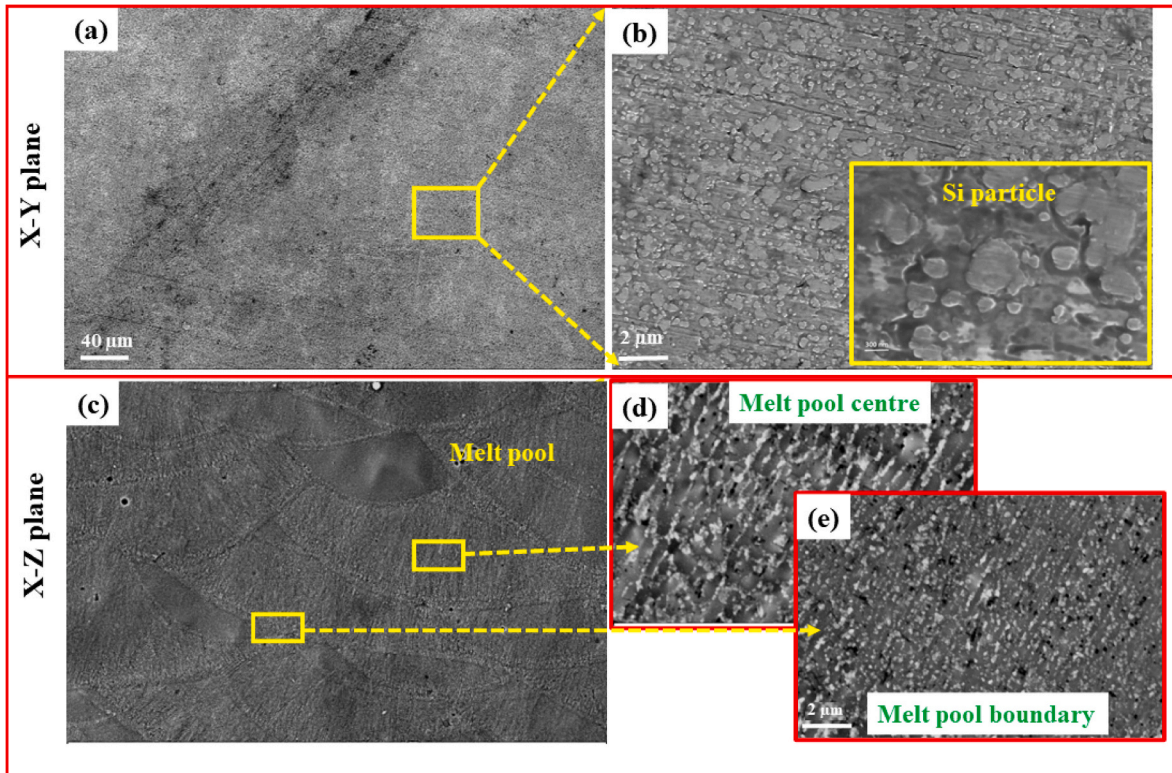

Fig. 7. Microstructure of T5 heat treated AlSi10Mg along (a and b) X–Y plane and (c and d) X-Z plane and e) melt pool boundary.
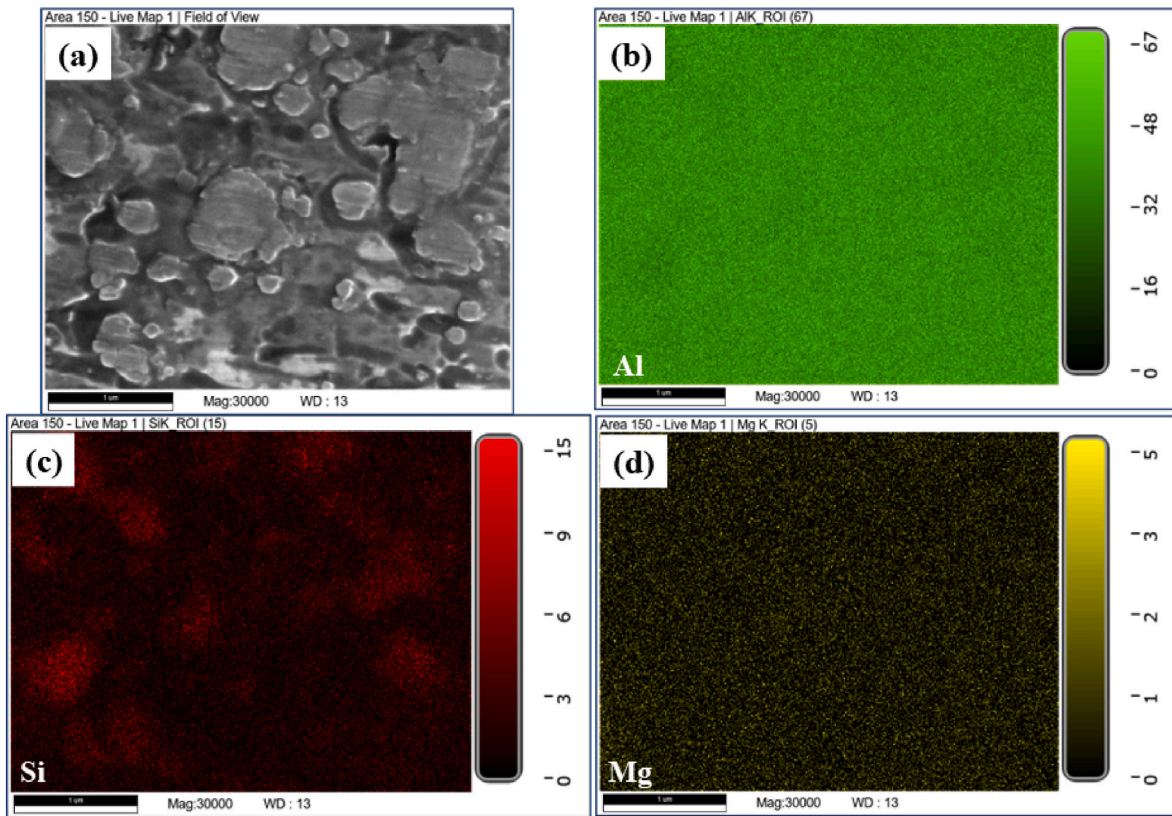
Fig. 8. Microstructure of X-Z plane (a) and elemental mapping of Al (b), Si (c) and Mg (d) for T5 heat-treated sample.
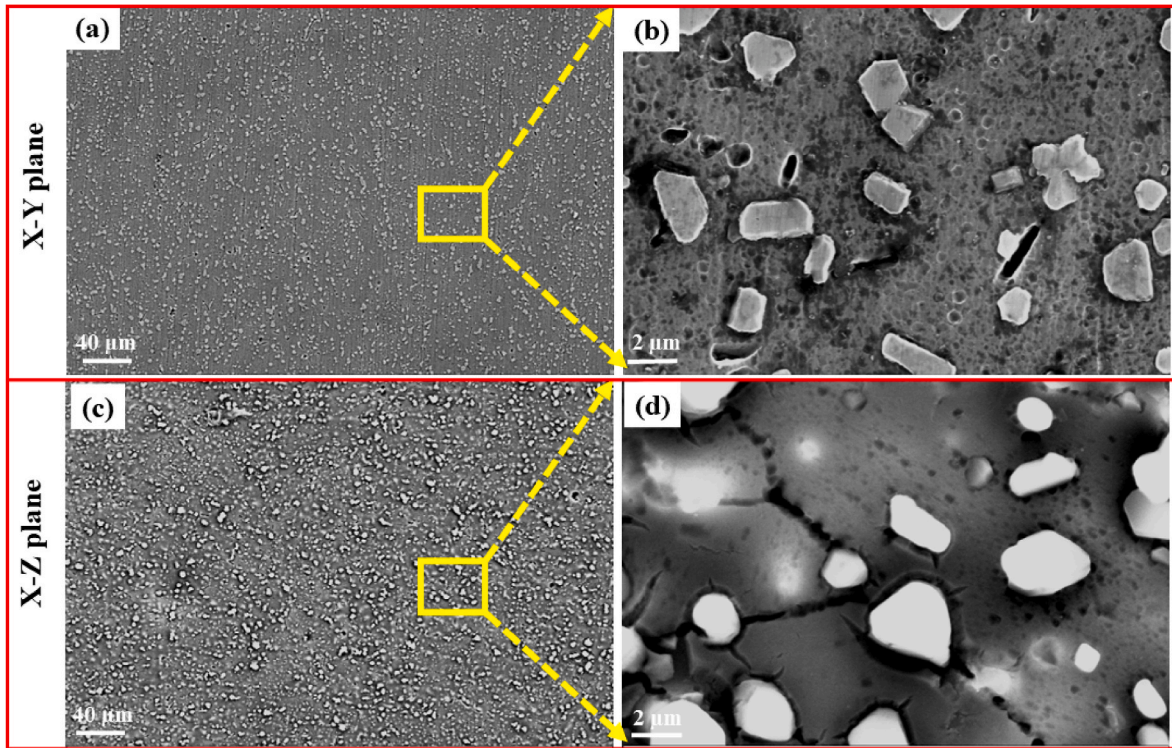

Fig. 9. Microstructure of T6 heat treated AlSi10Mg along (a, b) X–Y plane and (c, d) X-Z plane.

solution can result in minor Si phase precipitation within the α-Al matrix. As a result, eutectic Si fuses and accumulates in the α-Al matrix, leading to its softening and a subsequent decrease in strength [57].

Fig. 10 shows the presence of Si-particles in the microstructure. It is observed that compared to the T5 condition, T6 shows a relatively large Si-particle.
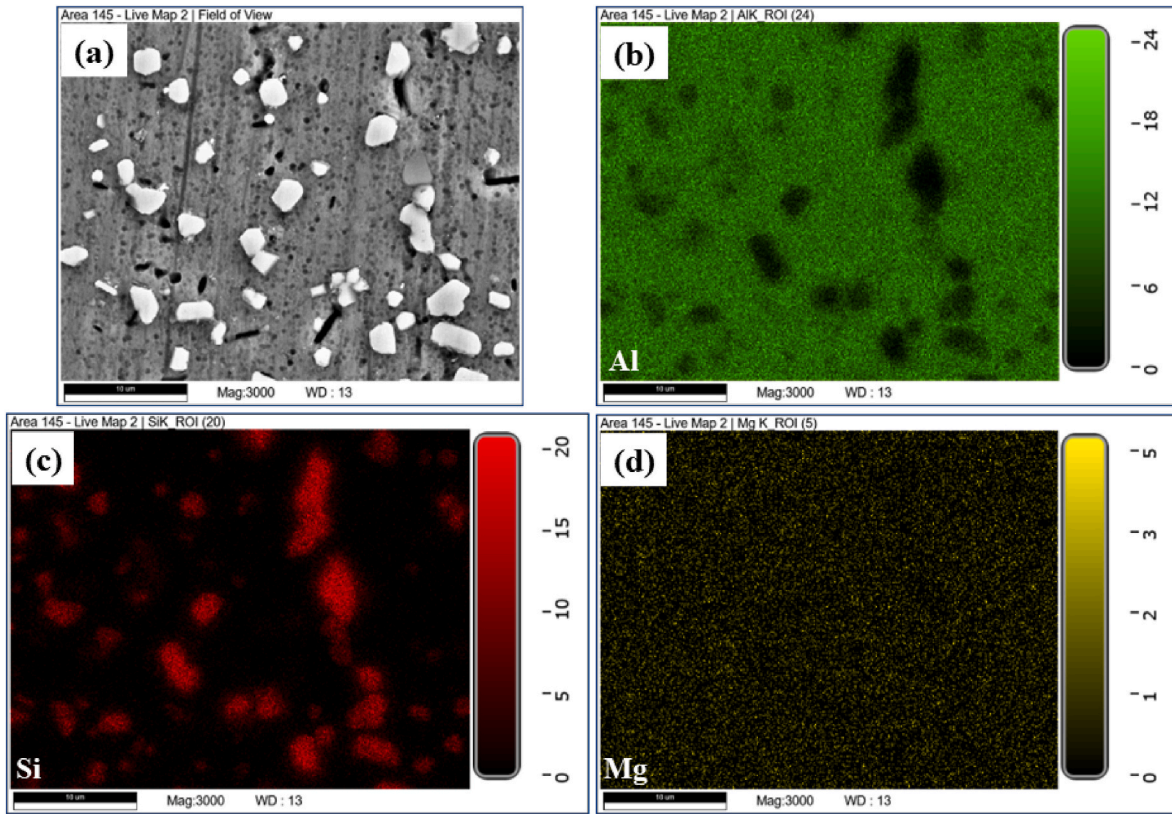
Fig. 10. Microstructure of X-Z plane (a) and elemental mapping of Al (b), Si (c) and Mg (d) for T6 heat-treated sample.
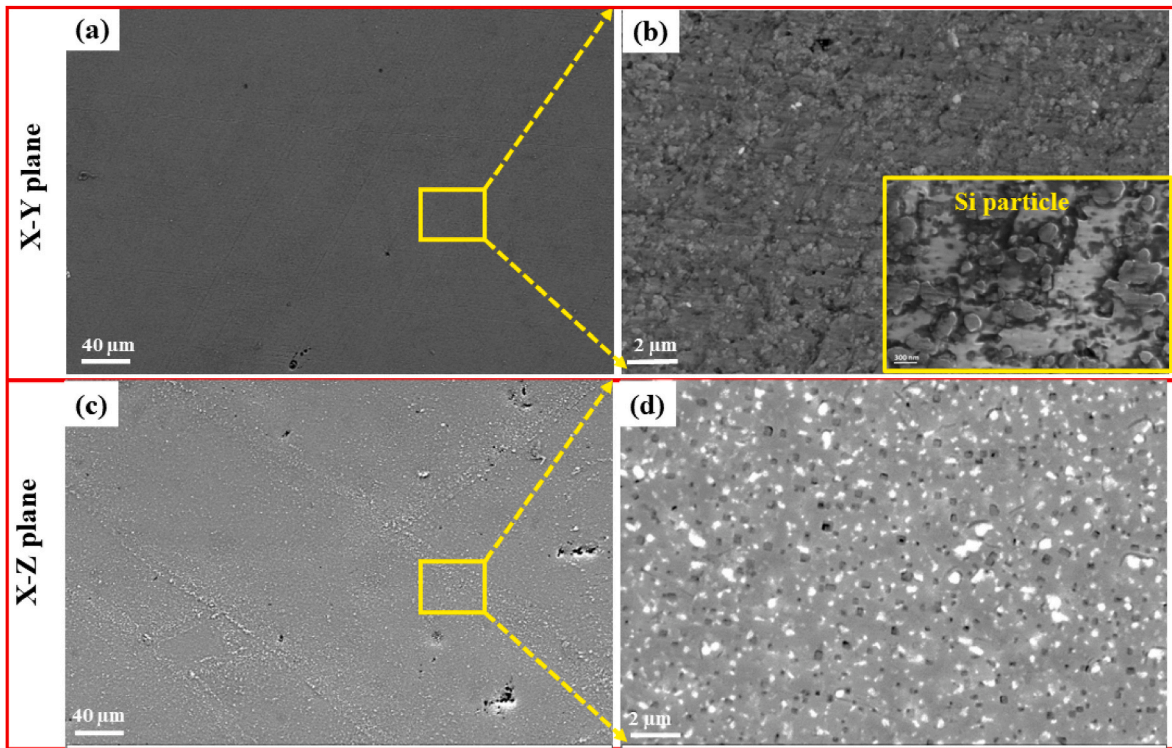

Fig. 11. Microstructure of SR treated AlSi10Mg along (a, b) X–Y plane and (c, d) X-Z plane.

Finally, The SR process implemented is designed to reduce the residual stress during the LPBF process. From Fig. 11, it is evident that SR heat-treated samples exhibit distinct microstructures compared to as-built conditions. After the SR heat treatment, melt pools disappear and the residual stress generated during the layer-by-layer process is reduced. The cellular α-Al dissolves, and the coarsening of Si particles is

observed in the SR condition as shown in Fig. 11 (b) inset. The coarsening of eutectic Si is also noticed. The initiation of Si spheroidization and the expansion of these particles contribute to the progressive dissolution of the continuous network. As per the earlier literature, the SR condition, enhances the mechanical properties and increases the ductility [58]. Fig. 12, featuring EDS mapping, reveals the distribution of Si particles throughout the microstructure, suggesting the coarsening of Si particles into the Al cell matrix.

3.2. XRD analysis of as-built and heat-treated samples

Fig. 13(a) shows the XRD results for both the as-built samples and those subjected to various heat treatment conditions. The detected diffraction peaks match the Al, Si, and Mg_2Si phases, as identified by their corresponding JCPDS patterns: 89–2837 for Al, 89–5012 for Si, and 01–1192 for Mg_2Si [70]. Notably, the XRD patterns of the heat-treated specimens exhibit Si peaks with higher intensities than the as-printed samples, signifying the presence of precipitation of Si particles following heat treatment. Also, as-built samples indicate the presence of Mg_2Si at a Bragg angle of ~99°. Mg_2Si precipitates are rarely observed during the LPBF process. This could result from the self-quenching effect caused by the layer-by-layer deposition. Moreover, the subsequent layers' rapid cooling and heating cycles lead the samples to promote the formation of Mg_2Si precipitates. During the T6 heat treatment, we observe a Si peak intensification, indicating a significant amount of Si within the α-Al matrix due to the elevated solution treatment temperature (Fig. 13(b)). This subsequently results in a reduced Si content within the α-Al matrix. Furthermore, Mg_2Si peaks are now evident in the all-heat-treated samples. Zhou et al. [63] stated that the presence of the Al–Mg_2Si eutectic network and the in-situ Mg_2Si precipitate formation enhances the mechanical properties of the alloy.

In addition, Fig. 13(b) illustrates the displacement of the Si peak in the heat-treated samples (T5, T6, and SR) compared to as-built samples.

The higher intensity observed for the T6 samples from Section 3.1, due to the microstructure analysis (formation of Si particles), might cause the increase in Si peak at a Bragg angle of ~29°. Generally, as-built samples exhibit the tensile residual stress due to higher temperatures and sudden cooling. Tensile residual stresses negatively impact mechanical properties, including fatigue and wear resistance. After heat treatment, XRD peaks at a Bragg angle of ~29° shift towards higher angles, indicating the tensile stress relaxation or the induction of compressive residual stresses. To understand this, the samples were subjected to the residual analysis by XRD using the $Sin^2\Psi$ method. The as-built samples exhibit tensile residual stress around 30 MPa, whereas heat-treated samples show compressive residual stress of -15 ± 2.2, -7 ± 1.5, and -12 ± 1.8 MPa for T6, T5, and SR conditions.

3.3. Microhardness

Fig. 14 displays the hardness levels of different heat-treated samples, with the microhardness of the as-built sample being ~36 HV. Following the T5 heat treatment, there is a notable 62.5% reduction in microhardness, resulting in a value of 85 HV. Similarly, the T6 and SR heat-treated samples exhibit 58% and 48% reductions, respectively, compared to the as-built sample. The as-built samples exhibited increased hardness, attributed to Si particles and a refined α-Al cellular structure, resulting from the rapid cooling manufacturing process [57]. In contrast, the α-Al cellular structure is lost, and the Si particles coarsen, leading to a lower density of grain boundaries, which tends to decrease the hardness values [71]. Notably, the SR heat-treated sample exhibits a notable reduction in hardness compared to the as-built sample, which could be attributed to the coarsening of the microstructure following heat treatment, as discussed in Section 3.1. In addition, as-built samples typically undergo rapid solidification rates, resulting in a fine and non-equilibrium microstructure. This can result in metastable phases or an increased number of defects like dislocations or vacancies. Heat
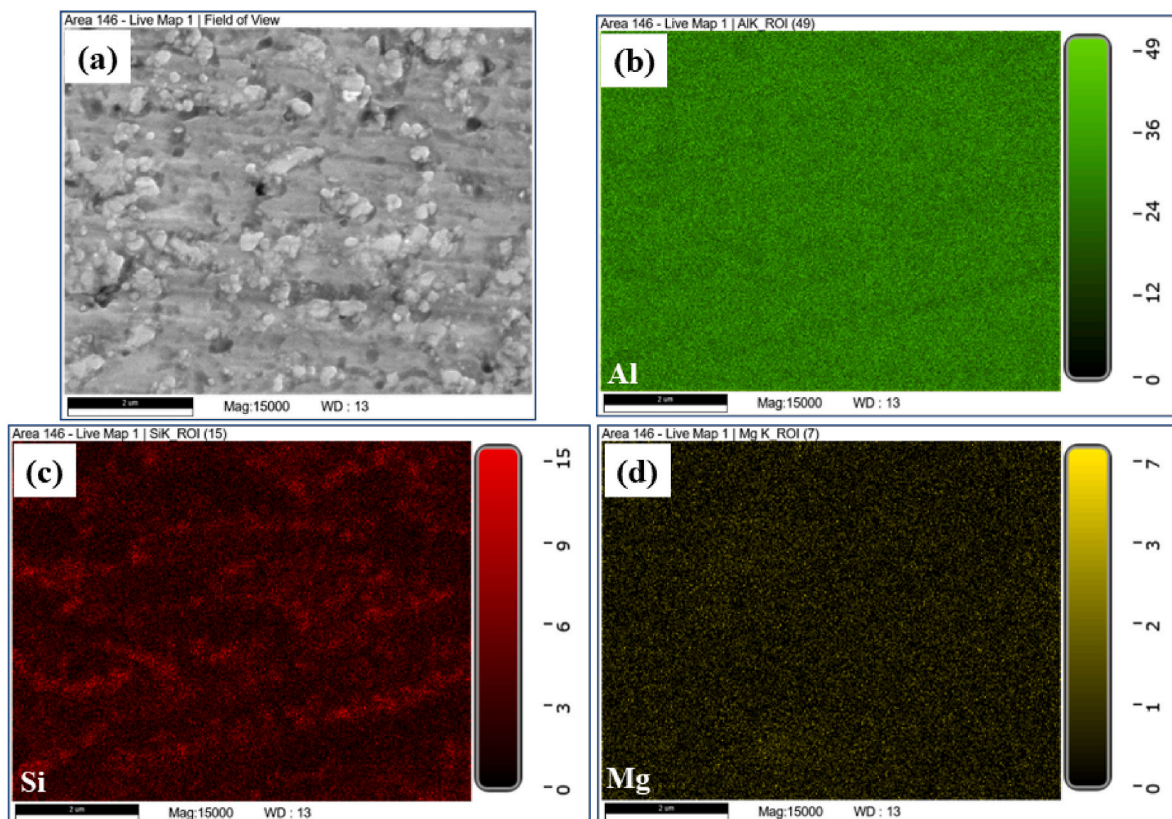

Fig. 12. Microstructure of X-Z plane (a) and elemental mapping of Al (b), Si (c) and Mg (d) for SR heat-treated sample.
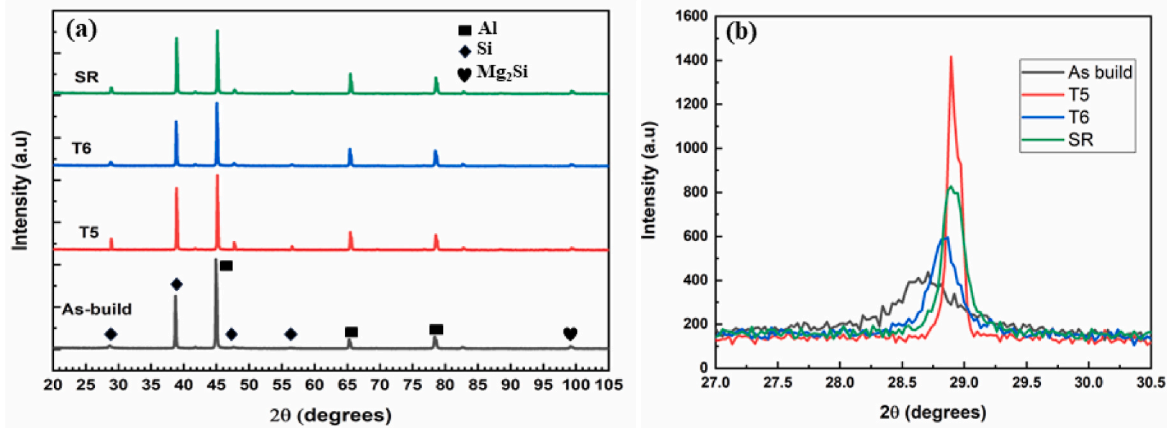
Fig. 13. (a) XRD of different heat-treated condition and (b) magnified image of XRD for Si-311 plane ($2\theta = \sim29°$).
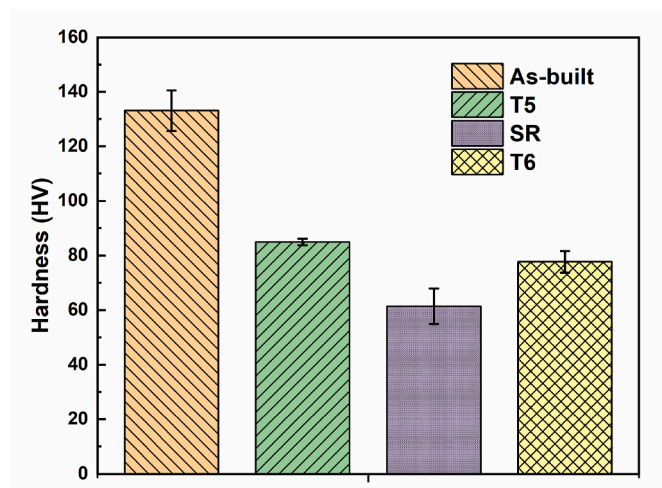

Fig. 14. Hardness of as-built and heat-treated condition.

treatment facilitates the relaxation of residual stresses and a decrease in defect density, ultimately reducing the cold work on the samples. Consequently, the hardness of the heat-treated samples may be lower due to these factors.

3.4. Fretting wear

3.4.1. COF

3.4.1.1. At 10 N load. Fig. 15(a–c) illustrates how the COF varies with the number of cycles for both as-built and heat-treated samples. At first, the COF rises to the highest levels, signifying the occurrence of run-in wear, and then stabilizes after 2000 to 3000 cycles, eventually achieving a steady-state wear condition. Notably, the as-built samples exhibit a lower COF value of 0.59, while the heat-treated samples display COF values of 1.40, 1.41, and 1.44 for T5, T6, and SR samples, respectively (Fig. 15 (d)).

3.4.1.2. At 50 N load. The normal load was increased to 50 N to understand the fretting wear behavior further. Fig. 15 (b) shows the changes in the COF relative to the number of cycles for both as-built and heat-treated samples when subjected to a 50 N load. The average COF values for as-built, T5, T6, and SR samples are 0.26, 0.34, 0.33, and 0.39, respectively. Among the different heat treatment conditions, it's noteworthy that the as-built samples consistently exhibit lower COF values.

3.4.1.3. At 100 N load. Fig. 15(c) depicts how the COF varies with the number of cycles for both as-built and heat-treated samples under a load of 100 N. The average COF values for as-built, T5, T6, and SR samples are 0.12, 0.17, 0.16, and 0.16, respectively. Just as observed in the 10 and 50 N loading conditions, it is evident that the as-built samples consistently exhibit lower COF values even under the 100 N loading condition.

3.4.2. Wear volume loss

3.4.2.1. At 10, 50 and 100 N load. Fig. 16 compares wear volume loss between the as-built and heat-treated conditions. Across all loading conditions, the as-built samples consistently exhibit lower volume loss. For instance, at a 10 N load, the as-built samples display a volume loss of 0.00011 m^3, while the heat-treated samples show higher volume losses of 0.0013, 0.0022, and 0.0018 m^3 for T5, SR and T6 respectively. Similarly, at a 50 N load, the as-built samples experience a volume loss of 0.0003 m^3, whereas the heat-treated samples demonstrate higher volume losses of 0.0002, 0.002, and 0.0005 m^3 for T5, SR, and T6 respectively. At a 100 N load, the as-built samples exhibit a volume loss of 0.0069 m^3, whereas the heat-treated samples showcase higher volume losses of 0.0009, 0.0019, and 0.0016 m^3 for T5, SR, and T6, respectively.

As observed from Fig. 16, the as-built samples consistently exhibit lower volume loss, whereas the SR samples consistently show higher volume loss regardless of the normal load.

3.4.3. Worn morphology

3.4.3.1. At 10 N load. The worn morphologies analysis of both the as-built and heat-treated samples are presented in Figs. 8–10, considering loads of 10, 50, and 100 N at a frequency of 15 Hz. The examination of these worn morphologies and surface topography offers insights into the wear mechanisms occurring during fretting. Fig. 17 provides clear evidence of distinctions between the conditions. In the as-built samples, surface features include delamination and grooves, while the heat-treated samples exhibit cracks, cavities, delamination, and grooves. Note that the presence of cavities acts as crack initiation that causes structural part damage, leading to reduced strength, stiffness, and catastrophic failures, a commonly observed mechanism in LPBF metallic glasses and concrete structures [72–75]. As-built samples exhibit a smoother surface compared to the heat-treated samples. The worn surface topography is detailed in Fig. 17(c–f, i, l). Heat-treated samples demonstrated a significant interaction area than the as-built samples, resulting in a lower wear volume loss observed in the latter. A noticeable difference is observed in the topography: the as-built samples exhibit a circular pattern, whereas the heat-treated samples display an elliptical
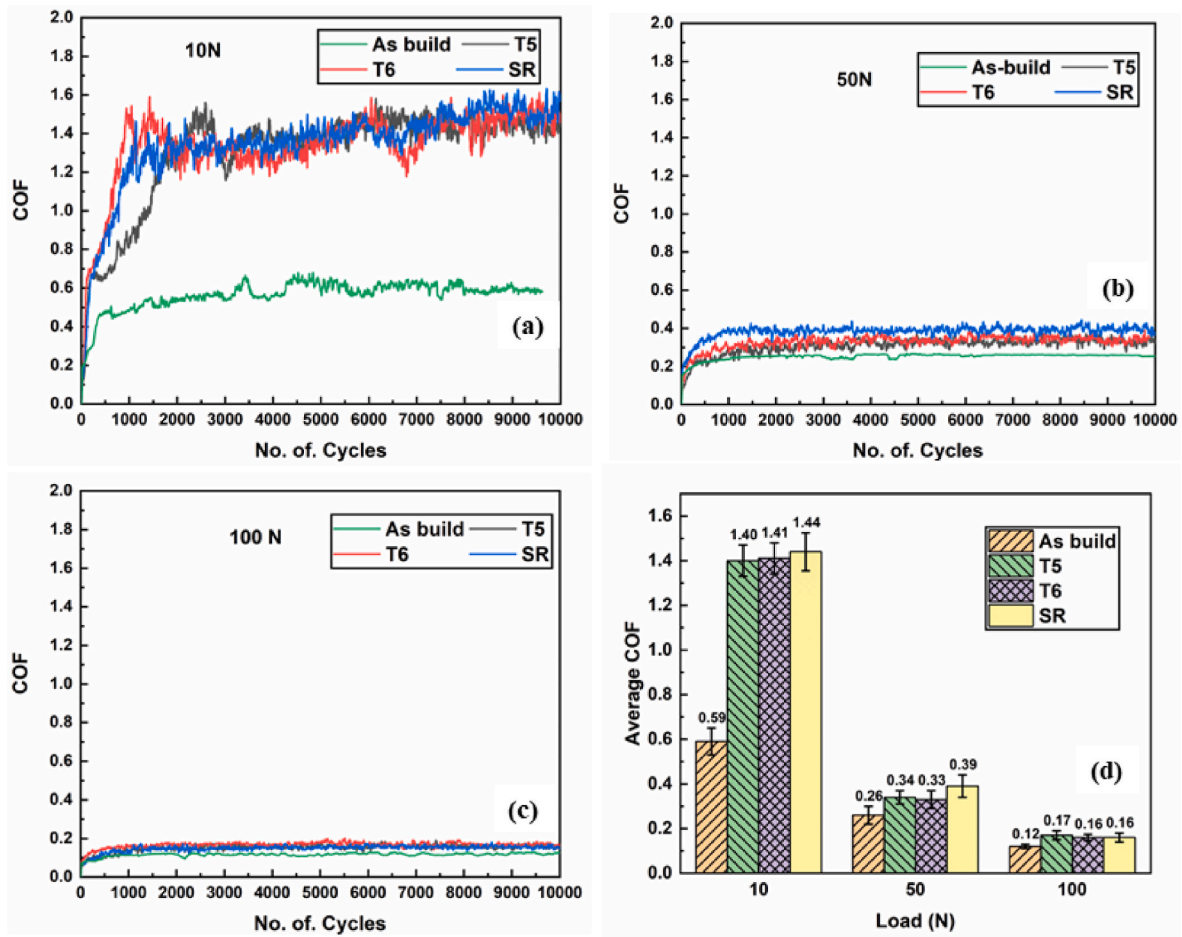
Fig. 15. COF of (a) 10 N, (b) 50 N and (c) 100 N loading and (d) average COF.
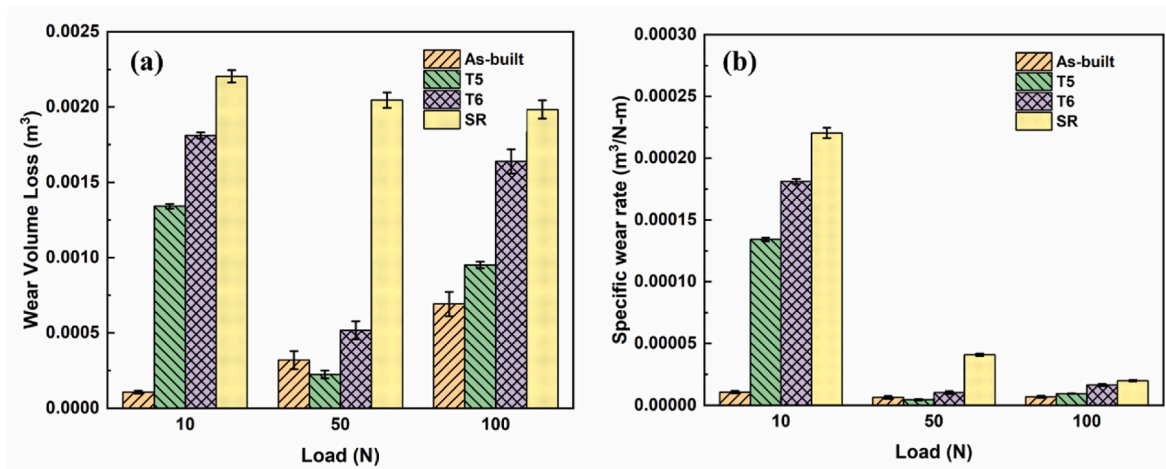

Fig. 16. (a) Wear volume loss and (b) specific wear rate, of as-built and heat-treated samples.

morphology.

3.4.3.2. At 50 N load. Fig. 18 depicts the worn morphologies of both the as-built and heat-treated samples under a normal load of 50 N are depicted. It is noticeable that the as-built samples exhibit a smaller worn surface area (interaction area) when compared to the heat-treated condition. The as-built and T5-conditioned samples display a circular morphology, while the T6 and SR samples exhibit an elliptical

morphology. Furthermore, the as-built samples exhibit smaller grooves on the worn surface, whereas the heat-treated samples show signs of delamination or cracks at the edges. Additionally, it is worth noting that worn debris is notably present in the worn morphologies of the heat-treated samples.

3.4.3.3. At 100 N load. Upon increasing the normal load to 100 N, the samples show relatively smaller worn surfaces compared to 10 and 50 N
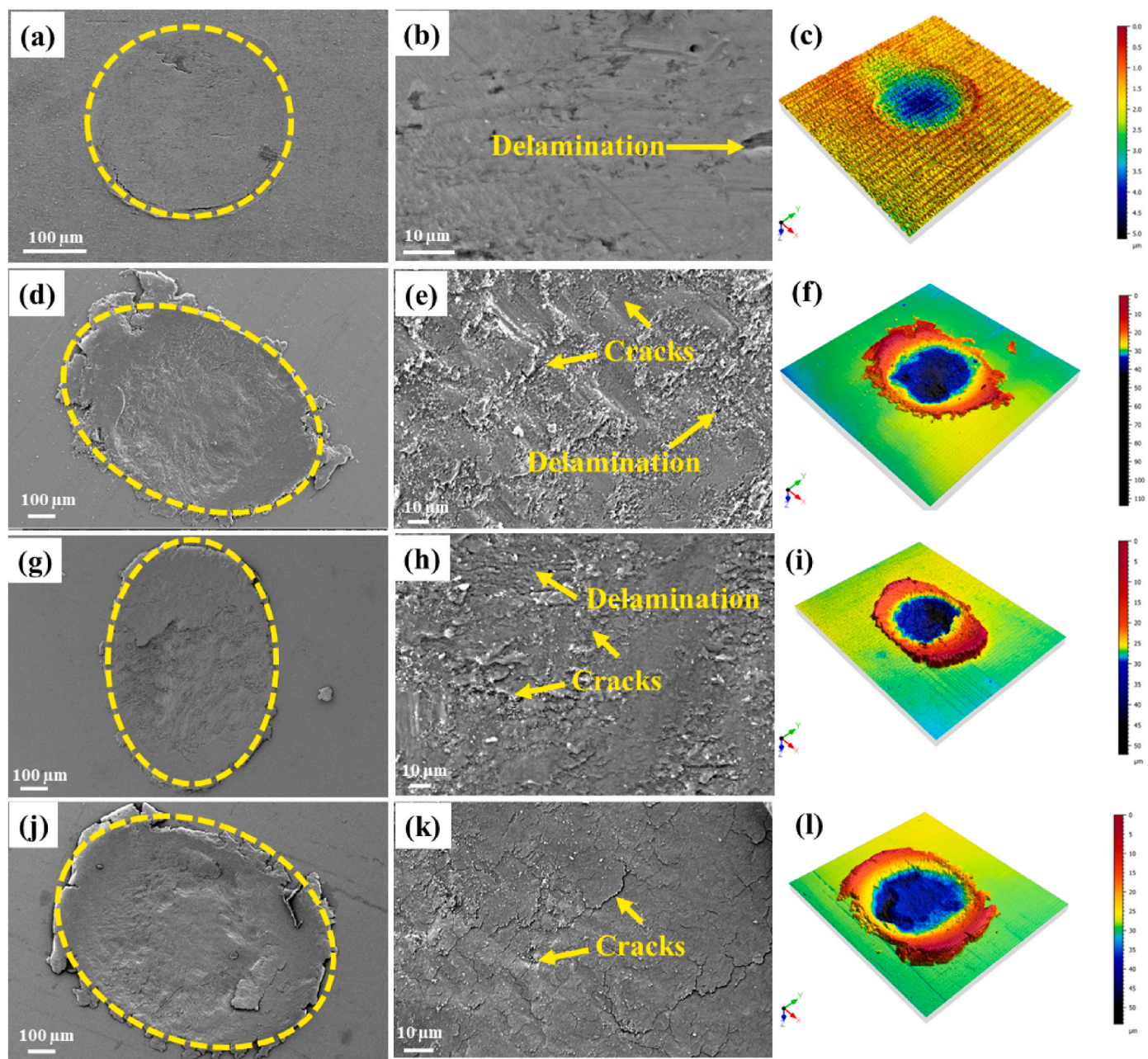
Fig. 17. Worn morphologies (at 200x and 1500x magnification) and 3D optical profilometry images of (a–c) as-built, (d–f) T5, (g–i) T6, and (j–l) SR after 10 N loading.

loading conditions. Fig. 19 provides insight into the worn morphologies of the as-built and heat-treated conditions. Similar to the 10 and 50 N loading conditions, the as-built sample demonstrates a smaller wear scar diameter than the heat-treated condition. In terms of morphology, the as-built sample maintains a circular shape, whereas the heat-treated samples exhibit a slightly elliptical morphology. Furthermore, the worn morphology of the as-built samples appears relatively smooth, unlike the T5 samples, which show a cluster of wear debris. The T6 and SR samples, on the other hand, exhibit severe cracks and delamination at the worn surface.

3.4.4. Oxygen mapping of worn surface

Fig. 20 illustrates the oxygen variation in relation to different loading conditions for both as-built and heat-treated samples. Notably, as-built samples consistently exhibit a limited oxygen content of less than 2 wt % across all loading conditions. In contrast, heat-treated samples display

a higher oxygen concentration on the worn surface when subjected to a 10 N loading condition, with values of 38.5, 41.2, and 34.5% observed for T5, T6, and SR respectively. However, when the normal load is increased to 50 and 100 N, both as-built and heat-treated samples demonstrate lower oxygen concentrations, remaining below 2%.

4. Wear mechanism

In general, fretting wear under atmospheric conditions is significantly influenced by the applied normal load [33,76]. To gain insights into wear behavior under various normal loads, this study investigates different levels of normal loads: 10, 50, and 100 N.

Initially, when subjected to a 10 N loading condition, the wear scar diameter and cross-sectional wear scar analysis (as shown in Figs. 17–19) reveal that as-built samples exhibit lower wear volume loss than heat-treated conditions. This suggests that as-built samples
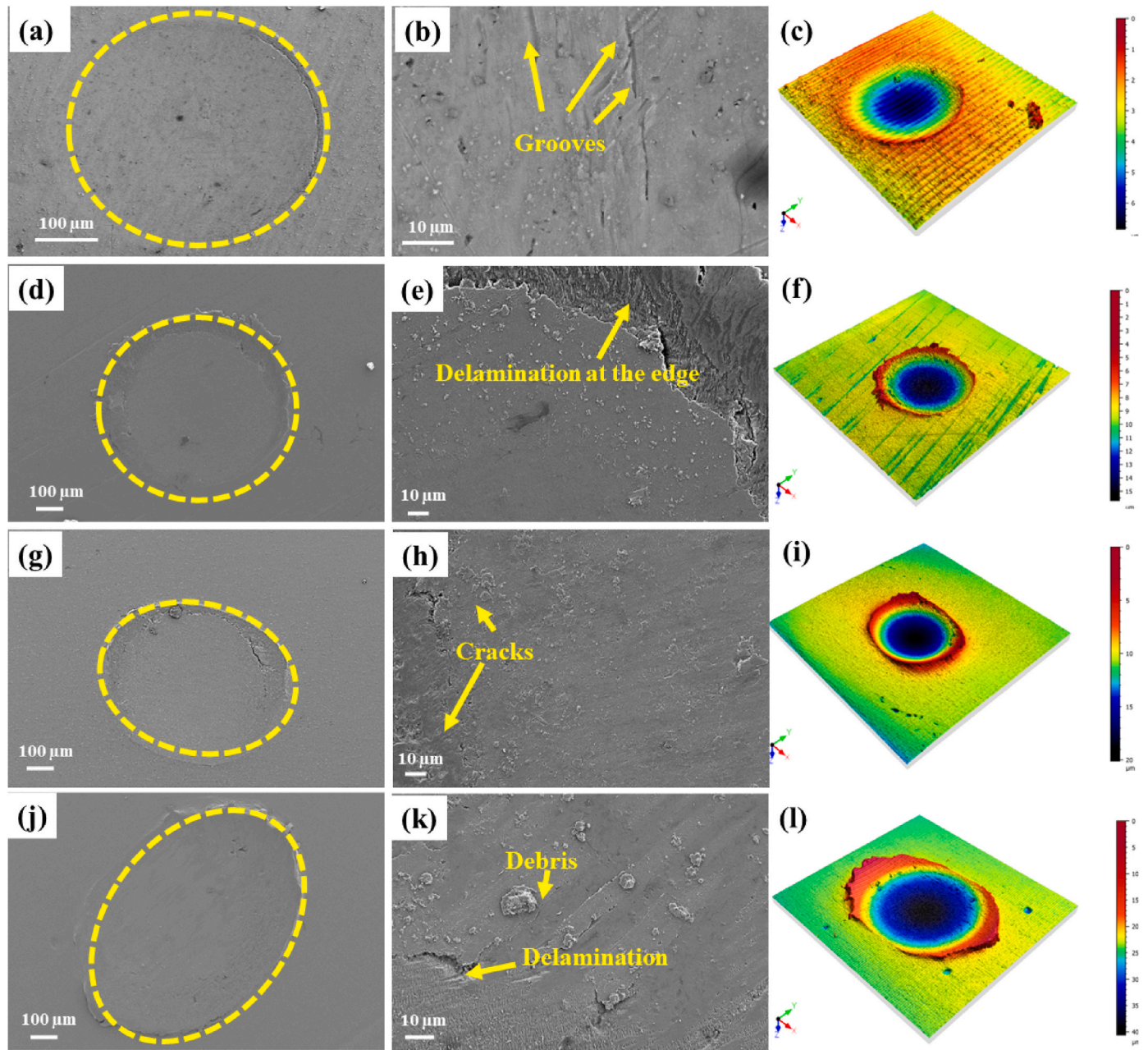
Fig. 18. Worn morphologies (at 200x and 1500x magnification) and 3D optical profilometry images of (a–c) as-built, (d–f) T5, (g–i) T6, and (j–l) SR after 50 N loading.

demonstrate superior fretting wear resistance when contrasted with heat-treated samples (specifically, T5, T6, and SR). The as-built samples exhibit limited grooves parallel to the fretting direction, which is indicative of mild abrasive wear. In contrast, heat-treated samples at the 10 N loading condition exhibit surface cracks and delamination. Furthermore, an elliptical scar is observed on the heat-treated samples. A transition from circular to elliptical scars typically indicates high shear and plasticity [77,78]. Figs. 17–19 (f, i, l) illustrate that the heat-treated samples exhibit more pronounced ploughing, resulting in a plunging effect at the edges, as evident from 3D profilometry and worn morphology analysis. This indicates the occurrence of plastic deformation during the fretting testing of heat-treated samples. The morphology analysis indicates that the surface of as-built samples remains relatively smooth due to higher hardness (~135 HV). On the other hand, heat-treated samples exhibit crack formation at the sliding surface and edges, potentially due to higher stress concentration at the interface

(stick-slip interface) [77].

EDS analysis reveals a clear correlation between loading conditions and oxygen content in the tested samples. As-built samples consistently maintain a low oxygen content, whereas heat-treated samples accumulate more oxygen on worn surfaces, particularly under a 10 N load. However, oxygen concentration decreases at higher loads of 50 and 100 N. The concentration of oxygen content is notably higher in the heat-treated samples, as discussed in Section 3.4.4, signifying severe fretting damage. The higher oxygen concentration at the 10 N loading condition may be attributed to the formation of worn debris, followed by sliding on the debris under pressure, resulting in oxide patches on the worn surface. This indicates oxidative, adhesive and abrasive wear in heat-treated samples subjected to the 10 N loading condition, contributing to higher coefficients of friction values observed for heat-treated samples (as discussed in Section 3.4.1) compared to as-built samples.

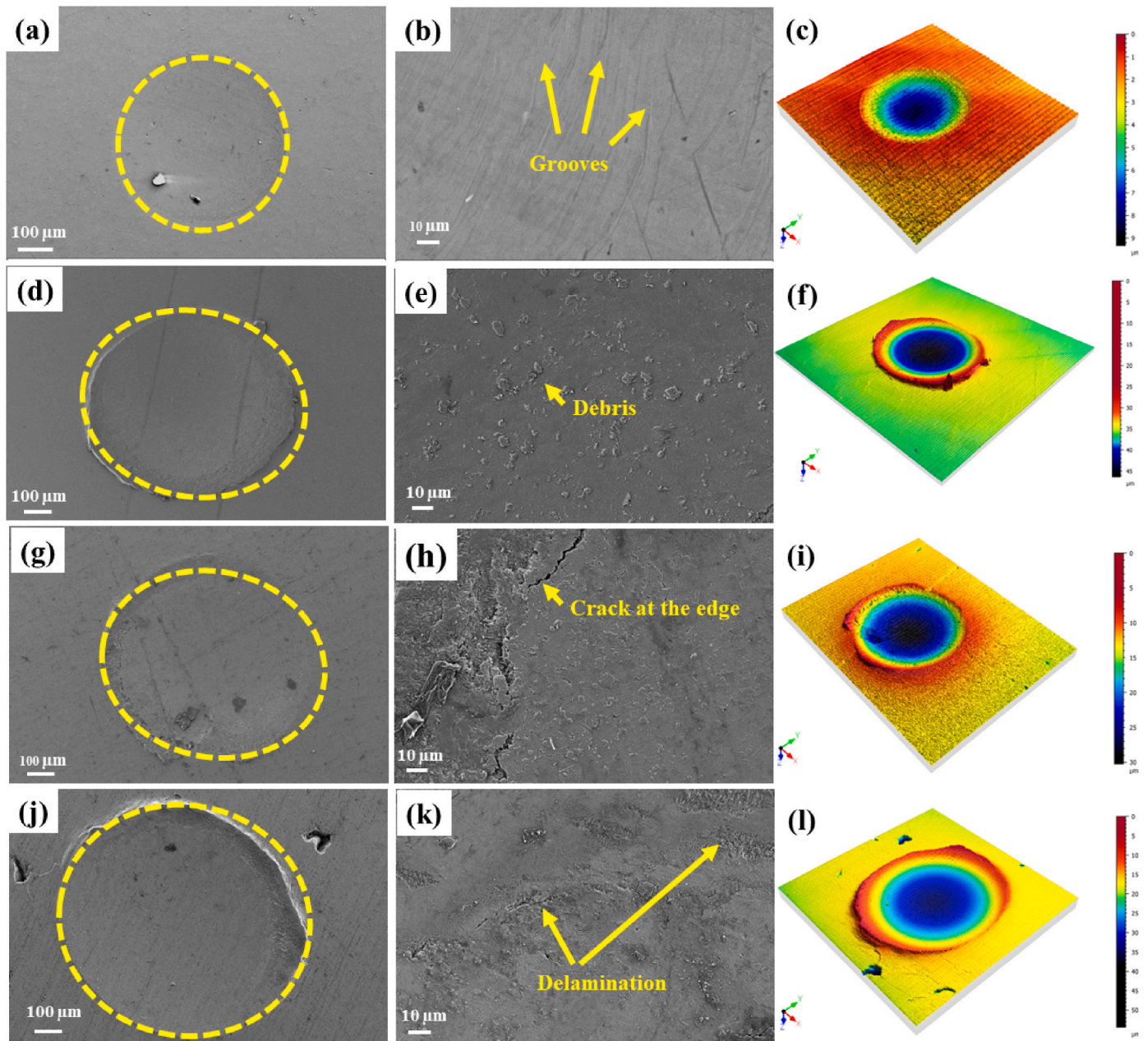Under higher normal loading conditions of 50 and 100 N, both as-

Fig. 19. Worn morphologies (at 200x and 1500x magnification) and 3D optical profilometry images of (a–c) as-built, (d–f) T5, (g–i) T6, and (j–l) SR after 100 N loading.

built and heat-treated samples exhibit lower oxygen concentration and relatively smaller grooves on the worn surface, indicating abrasive wear. A distinct stick regime is observed in heat-treated samples (see Figs. 17–19 (f, i, l)). The presence of cracks or delamination between the stick and slip (worn surface to edge) regime suggests adhesive wear under 50 and 100 N loading conditions. This indicates the partial-slip regime. The presence of the partial slip regime aligns with the notable lack of tribo-oxidation in the heat-treated samples subjected to higher loads [79]. The absence of relative slippage at the contact center implies minimal debris release, and the constant static contact in the central region reduces the opportunity for air to access the contact area. At higher loads (50 and 100 N), a reduction in contact pressure is due to the transition from gross slip to partial slip, which consequently lowers the COF. This is supported by the analysis of worn morphology. This aligns with the lower COF values observed for 50 and 100 N loading conditions compared to 10 N loading. Due to this, the wear volume loss and specific wear rate are also reduced at higher loads. The worn surface analysis and COF measurements collectively indicate abrasive wear for as-built and heat-treated samples under 50 and 100 N loading conditions.

To summarize, as-built samples demonstrate higher wear resistance across all loading conditions, likely attributable to their hierarchical microstructure and greater hardness. However, at higher loading conditions, the effectiveness of as-built samples is nearly on par with heat-treated samples.

5. Conclusions

AlSi10Mg samples were fabricated using the LPBF process and subjected to comprehensive mechanical and microstructural analysis, including hardness assessment, XRD, and SEM. Subsequently, a fretting wear investigation was carried out on as-built and heat-treated AlSi10Mg samples under ambient temperature conditions, employing
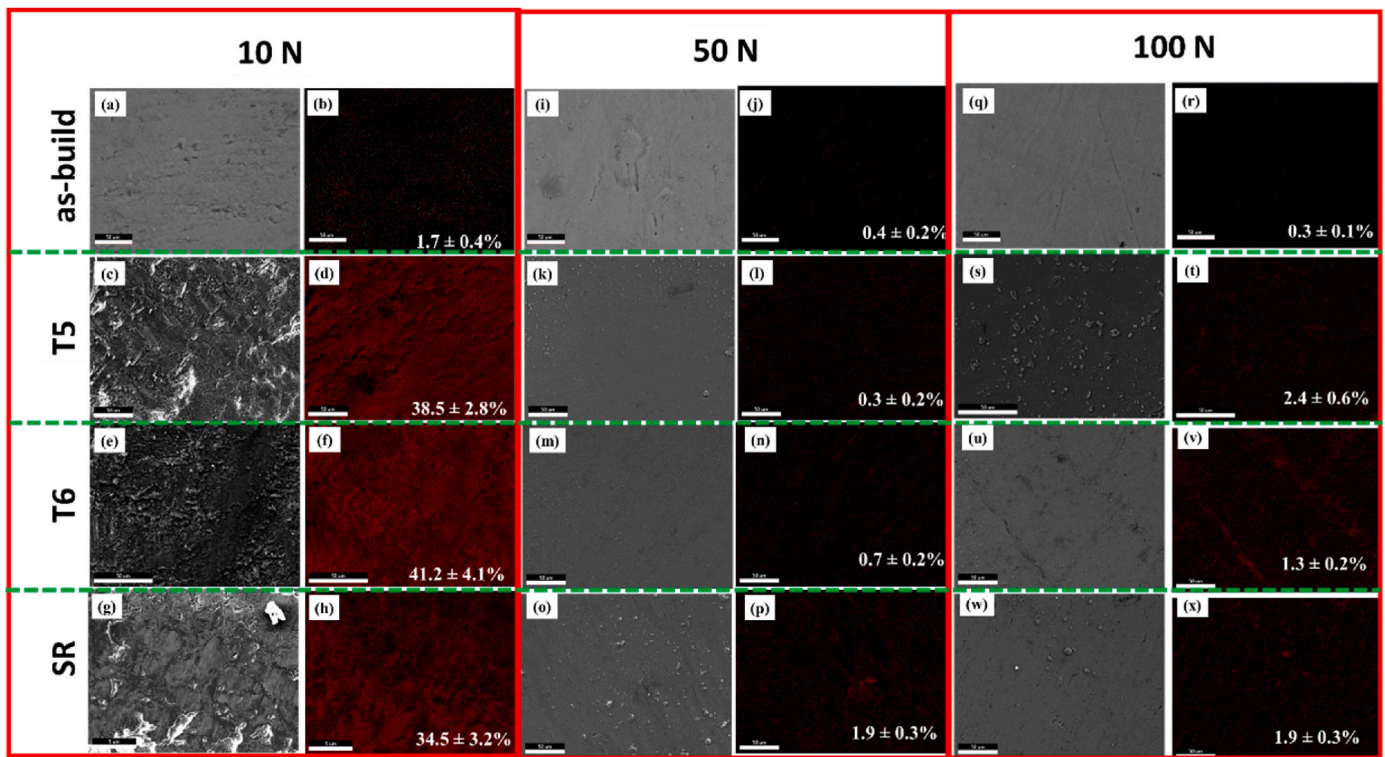
Fig. 20. EDS map of Oxygen for as built and heat treated subjected to 10, 50 and 100 N loading condition.

varying normal loading conditions. Worn morphology, oxygen distribution mapping, and wear volume loss were examined using SEM, EDS, and 3D optical profilometry. The following conclusions have been drawn based on the results of the aforementioned analysis.

1. From microstructural analysis, as-built samples exhibit a hierarchical microstructure at the melt pool center and boundary. In contrast, samples subjected to T5 and T6 heat treatment conditions display a finer microstructure characterized by Si particles and loss of α-Al cellular structure. SR samples exhibit Si particles in conjunction with features reminiscent of the as-built structure.
2. COF was lower for as-built samples across all the fretting conditions, whereas heat-treated samples showed higher COF than as-built samples due to changes in the microstructure and lower hardness.
3. Wear volume analysis also indicates lower loss for as-built samples at 10, 50, and 100 N loading conditions. Whereas, heat-treated samples show higher wear volume loss due to lower hardness and the absence of α-Al cell structure.
4. Based on the worn morphology and EDS analysis, it is concluded that as-built samples show mild abrasive wear across all loading conditions. In contrast, heat-treated samples (T5, T6, and SR) show oxidation, adhesion, and abrasive wear at 10 N loading condition, and in other loading conditions (50 and 100 N), oxidation was not observed, and severe adhesion wear due to partial slip regime.
5. XRD analysis reveals the as-built samples exhibit tensile residual stress, whereas heat-treated samples show compressive residual stress for different heat-treated samples.

Data availability

No data was used for the research described in the article.

Declaration of competing interest

The authors declare that they have no known competing financial interests or personal relationships that could have appeared to influence the work reported in this paper.

References

[1] Panesar A, Ashcroft I, Brackett D, Wildman R, Hague R. Design framework for multifunctional additive manufacturing: coupled optimization strategy for structures with embedded functional systems. Addit Manuf 2017;16:98–106. https://doi.org/10.1016/j.addma.2017.05.009.

[2] Maskery I, Hussey A, Panesar A, Aremu A, Tuck C, Ashcroft I, et al. An investigation into reinforced and functionally graded lattice structures. J Cell Plast 2017;53:151–65. https://doi.org/10.1177/0021955X16639035.

[3] Panesar A, Brackett D, Ashcroft I, Wildman R, Hague R. Hierarchical remeshing strategies with mesh mapping for topology optimisation. Int J Numer Methods Eng 2017;111:676–700. https://doi.org/10.1002/nme.5488.

[4] Vaithilingam J, Saleh E, Wildman RD, Hague RJM, Tuck CJ. Optimisation of substrate angles for multi-material and multi-functional Inkjet printing. Sci Rep 2018;8:2–9. https://doi.org/10.1038/s41598-018-27311-6.

[5] Aboulkhair NT, Simonelli M, Parry L, Ashcroft I, Tuck C, Hague R. 3D printing of Aluminium alloys: additive Manufacturing of Aluminium alloys using selective laser melting. Prog Mater Sci 2019;106:100578. https://doi.org/10.1016/j.pmatsci.2019.100578.

[6] Valean C, Maravina L, Marghita M, Linul E, Razavi N, Berto F, et al. The effect of crack insertion for FDM printed PLA materials on Mode I and Mode II fracture toughness. In: Procedia structural integrity, vol. 28. Elsevier B.V; 2020. p. 1134–9. https://doi.org/10.1016/j.prostr.2020.11.128.

[7] Stoia DI, Marsavina L, Linul E. Mode I fracture toughness of polyamide and aluminide samples obtained by selective laser sintering additive process. Polymers 2020;12. https://doi.org/10.3390/polym12030640.

[8] Yeo I, Bae S, Amanov A, Jeong S. Effect of laser shock peening on properties of heat-treated Ti–6Al–4V manufactured by laser powder bed fusion. International Journal of Precision Engineering and Manufacturing - Green Technology 2021;8: 1137–50. https://doi.org/10.1007/s40684-020-00234-2.

[9] DebRoy T, Wei HL, Zuback JS, Mukherjee T, Elmer JW, Milewski JO, et al. Additive manufacturing of metallic components – process, structure and properties. Prog Mater Sci 2018;92:112–224. https://doi.org/10.1016/j.pmatsci.2017.10.001.

[10] Koelblin J, Hastie JC, Kartal ME, Siddiq A, Attallah MM. Deformation of AlSi10Mg parts manufactured by Laser Powder Bed Fusion: in-situ measurements incorporating X-ray micro computed tomography and a micro testing stage. Procedia Struct Integr 2021;35:168–72. https://doi.org/10.1016/j.prostr.2021.12.061.

[11] Xiao YK, Bian ZY, Wu Y, Ji G, Li YQ, Li MJ, et al. Effect of nano-TiB2 particles on the anisotropy in an AlSi10Mg alloy processed by selective laser melting. J Alloys Compd 2019;798:644–55. https://doi.org/10.1016/j.jallcom.2019.05.279.

[12] Yap CY, Chua CK, Dong ZL, Liu ZH, Zhang DQ, Loh LE, et al. Review of selective laser melting: materials and applications. Appl Phys Rev 2015;2:41101. https://doi.org/10.1063/1.4935926.

[13] Buchbinder D, Schleifenbaum H, Heidrich S, Meiners W, Bültmann J. High power selective laser melting (HP SLM) of aluminum parts. Phys Procedia 2011;12:271–8. https://doi.org/10.1016/j.phpro.2011.03.035.

[14] Seabra M, Azevedo J, Araújo A, Reis L, Pinto E, Alves N, et al. Selective laser melting (SLM) and topology optimization for lighter aerospace components. Procedia Struct Integr 2016;1:289–96. https://doi.org/10.1016/j.prostr.2016.02.039.

[15] Zhang X, Huang T, Yang W, Xiao R, Liu Z, Li L. Microstructure and mechanical properties of laser beam-welded AA2060 Al-Li alloy. J Mater Process Technol 2016;237:301–8. https://doi.org/10.1016/j.jmatprotec.2016.06.021.

[16] Rosenthal I, Stern A, Frage N. Microstructure and mechanical properties of AlSi10Mg parts produced by the laser beam additive manufacturing (AM) technology. Metallography, Microstructure, and Analysis 2014;3:448–53. https://doi.org/10.1007/s13632-014-0168-y.

[17] Thijs L, Kempen K, Kruth JP, Van Humbeeck J. Fine-structured aluminium products with controllable texture by selective laser melting of pre-alloyed AlSi10Mg powder. Acta Mater 2013;61:1809–19. https://doi.org/10.1016/j.actamat.2012.11.052.

[18] Giovagnoli M, Tocci M, Fortini A, Merlin M, Ferroni M, Migliori A, et al. Effect of different heat-treatment routes on the impact properties of an additively manufactured AlSi10Mg alloy. Mater Sci Eng, A 2021;802:140671. https://doi.org/10.1016/j.msea.2020.140671.

[19] Subramaniyan AK, Reddy AS, Mathias S, Shrivastava A, Raghupatruni P. Influence of post-processing techniques on the microstructure, properties and surface integrity of Al[sbnd]Si[sbnd]Mg alloy processed by laser powder bed fusion technique. Surf Coat Technol 2021;425. https://doi.org/10.1016/j.surfcoat.2021.127679.

[20] Sharma SK, Grewal HS, Saxena KK, Mohammed KA, Prakash C, Davim JP, et al. Advancements in the additive manufacturing of magnesium and aluminum alloys through laser-based approach. Materials 2022;15. https://doi.org/10.3390/ma15228122.

[21] Wang Z, Ummethala R, Singh N, Tang S, Suryanarayana C, Eckert J, et al. Selective laser melting of aluminum and its alloys. Materials 2020;13:1–67. https://doi.org/10.3390/ma13204564.

[22] Fiocchi J, Tuissi A, Biffi CA. Heat treatment of aluminium alloys produced by laser powder bed fusion: a review. Mater Des 2021;204. https://doi.org/10.1016/j.matdes.2021.109651.

[23] Salmi A, Atzeni E, Iuliano L, Galati M. Experimental analysis of residual stresses on AlSi10Mg parts produced by means of selective laser melting (SLM). Procedia CIRP 2017;62:458–63. https://doi.org/10.1016/j.procir.2016.06.030.

[24] Aboulkhair NT, Maskery I, Tuck C, Ashcroft I, Everitt NM. The microstructure and mechanical properties of selectively laser melted AlSi10Mg: the effect of a conventional T6-like heat treatment. Mater Sci Eng, A 2016;667:139–46. https://doi.org/10.1016/j.msea.2016.04.092.

[25] Wei P, Chen Z, Zhang S, Fang X, Lu B, Zhang L, et al. Effect of T6 heat treatment on the surface tribological and corrosion properties of AlSi10Mg samples produced by selective laser melting. Mater Char 2021;171. https://doi.org/10.1016/j.matchar.2020.110769.

[26] Zhuo L, Wang Z, Zhang H, Yin E, Wang Y, Xu T, et al. Effect of post-process heat treatment on microstructure and properties of selective laser melted AlSi10Mg alloy. Mater Lett 2019;234:196–200. https://doi.org/10.1016/j.matlet.2018.09.109.

[27] Fiocchi J, Tuissi A, Bassani P, Biffi CA. Low temperature annealing dedicated to AlSi10Mg selective laser melting products. J Alloys Compd 2017;695:3402–9. https://doi.org/10.1016/j.jallcom.2016.12.019.

[28] Rosenthal I, Shneck R, Stern A. Heat treatment effect on the mechanical properties and fracture mechanism in AlSi10Mg fabricated by additive manufacturing selective laser melting process. Mater Sci Eng, A 2018;729:310–22. https://doi.org/10.1016/j.msea.2018.05.074.

[29] Giovagnoli M, Tocci M, Fortini A, Merlin M, Ferroni M, Migliori A, et al. Effect of different heat-treatment routes on the impact properties of an additively manufactured AlSi10Mg alloy. Mater Sci Eng, A 2021;802. https://doi.org/10.1016/j.msea.2020.140671.

[30] Zhang X, Li L, Wen Z, Ban T, Li Z, Shi R, et al. Post-heat treatment of laser powder bed fusion fabricated Al–La–Mg–Mn alloy: on intermetallic morphology control and strength-ductility balance. Addit Manuf 2023;78:103863. https://doi.org/10.1016/j.addma.2023.103863.

[31] Raffeis I, Adjei-Kyeremeh F, Ewald S, Schleifenbaum JH, Bührig-Polaczek A. A combination of alloy modification and heat treatment strategies toward enhancing the properties of LPBF processed Hot working tool steels (HWTS). J Manuf Mater Process 2022;6. https://doi.org/10.3390/jmmp6030063.

[32] Pinto AL, Araújo JA, Talemi R. Effects of fretting wear process on fatigue crack propagation and life assessment. Tribol Int 2021;156:106787. https://doi.org/10.1016/j.triboint.2020.106787.

[33] Praveenkumar K, Swaroop S, Manivasagam G. Effect of multiple laser peening on microstructural, fatigue and fretting-wear behaviour of austenitic stainless steel. Surf Coat Technol 2022;443:128611. https://doi.org/10.1016/j.surfcoat.2022.128611.

[34] Mohrbacher H, Celis JP, Roos JR. Laboratory testing of displacement and load induced fretting. Tribol Int 1995;28:269–78. https://doi.org/10.1016/0301-679X(95)00005-O.

[35] Read N, Wang W, Essa K, Attallah MM. Selective laser melting of AlSi10Mg alloy: process optimisation and mechanical properties development. Mater Des 2015;65:417–24. https://doi.org/10.1016/j.matdes.2014.09.044.

[36] Weingarten C, Buchbinder D, Pirch N, Meiners W, Wissenbach K, Poprawe R. Formation and reduction of hydrogen porosity during selective laser melting of AlSi10Mg. J Mater Process Technol 2015;221:112–20. https://doi.org/10.1016/j.jmatprotec.2015.02.013.

[37] Zhang Y, Yang L, Chen T, Zhang W, Huang X, Dai J. Investigation on the optimized heat treatment procedure for laser fabricated IN718 alloy. Opt Laser Technol 2017;97:172–9. https://doi.org/10.1016/j.optlastec.2017.06.027.

[38] Aboulkhair NT, Maskery I, Ashcroft I, Tuck CJ. The role of powder properties on the processability of Aluminium alloys in selective laser melting Lasers in Manufacturing Conference 2015 the role of powder properties on the processability of Aluminium alloys in selective laser melting. In: Lasers in manufacturing conference 2015; 2015.

[39] Boschetto A, Bottini L, Veniali F. Roughness modeling of AlSi10Mg parts fabricated by selective laser melting. J Mater Process Technol 2017;241:154–63. https://doi.org/10.1016/j.jmatprotec.2016.11.013.

[40] Aboulkhair NT, Maskery I, Tuck C, Ashcroft I, Everitt NM. The microstructure and mechanical properties of selectively laser melted AlSi10Mg: the effect of a conventional T6-like heat treatment. Mater Sci Eng, A 2016;667:139–46. https://doi.org/10.1016/j.msea.2016.04.092.

[41] Anwar A Bin, Pham QC. Selective laser melting of AlSi10Mg: effects of scan direction, part placement and inert gas flow velocity on tensile strength. J Mater Process Technol 2017;240:388–96. https://doi.org/10.1016/j.jmatprotec.2016.10.015.

[42] Liu S, Zhu H, Peng G, Yin J, Zeng X. Microstructure prediction of selective laser melting AlSi10Mg using finite element analysis. Mater Des 2018;142:319–28. https://doi.org/10.1016/j.matdes.2018.01.022.

[43] Takata N, Kodaira H, Sekizawa K, Suzuki A, Kobashi M. Change in microstructure of selectively laser melted AlSi10Mg alloy with heat treatments. Mater Sci Eng, A 2017;704:218–28. https://doi.org/10.1016/j.msea.2017.08.029.

[44] Tradowsky U, White J, Ward RM, Read N, Reimers W, Attallah MM. Selective laser melting of AlSi10Mg: influence of post-processing on the microstructural and tensile properties development. Mater Des 2016;105:212–22. https://doi.org/10.1016/j.matdes.2016.05.066.

[45] Luven KU. Study of residual stresses in selective laser melting. 2016.

[46] Ponnusamy P, Rashid RAR, Masood SH, Ruan D, Palanisamy S. Mechanical properties of slm-printed aluminium alloys: a review. Materials 2020;13:1–51. https://doi.org/10.3390/ma13194301.

[47] Bastola N, Jahan MP, Rangasamy N, Rakurty CS. A review of the residual stress generation in metal additive manufacturing: analysis of cause, measurement, effects, and prevention. Micromachines 2023;14. https://doi.org/10.3390/mi14071480.

[48] Diniţă A, Neacşa A, Portoacă AI, Tănase M, Ilinca CN, Ramadan IN. Additive manufacturing post-processing treatments, a review with emphasis on mechanical characteristics. Materials 2023;16. https://doi.org/10.3390/ma16134610.

[49] Tabatabaeian A, Ghasemi AR, Shokrieh MM, Marzbanrad B, Baraheni M, Fotouhi M. Residual stress in engineering materials: a review. Adv Eng Mater 2022;24. https://doi.org/10.1002/adem.202100786.

[50] Yadollahi A, Shamsaei N. Additive manufacturing of fatigue resistant materials: challenges and opportunities. Int J Fatig 2017;98:14–31. https://doi.org/10.1016/j.ijfatigue.2017.01.001.

[51] Ponnusamy P, Rashid RAR, Masood SH, Ruan D, Palanisamy S. Mechanical properties of slm-printed aluminium alloys: a review. Materials 2020;13:1–51. https://doi.org/10.3390/ma13194301.

[52] Özer G, Tarakçi G, Yilmaz MS, Öter Z, Sürmen Ö, Akça Y, et al. Investigation of the effects of different heat treatment parameters on the corrosion and mechanical properties of the AlSi10Mg alloy produced with direct metal laser sintering. Mater Corros 2020;71:365–73. https://doi.org/10.1002/maco.201911171.

[53] Van Cauwenbergh P, Samaee V, Thijs L, Nejezchlebová J, Sedlák P, Iveković A, et al. Unravelling the multi-scale structure–property relationship of laser powder bed fusion processed and heat-treated AlSi10Mg. Sci Rep 2021;11:1–15. https://doi.org/10.1038/s41598-021-85047-2.

[54] Iturrioz A, Gil E, Petite MM, Garciandia F, Mancisidor AM, San Sebastian M. Selective laser melting of AlSi10Mg alloy: influence of heat treatment condition on mechanical properties and microstructure. Weld World 2018;62:885–92. https://doi.org/10.1007/s40194-018-0592-8.

[55] Zhang C, Zhu H, Liao H, Cheng Y, Hu Z, Zeng X. Effect of heat treatments on fatigue property of selective laser melting AlSi10Mg. Int J Fatig 2018;116:513–22. https://doi.org/10.1016/j.ijfatigue.2018.07.016.

[56] Aboulkhair NT, Maskery I, Tuck C, Ashcroft I, Everitt NM. Improving the fatigue behaviour of a selectively laser melted aluminium alloy: influence of heat treatment and surface quality. Mater Des 2016;104:174–82. https://doi.org/10.1016/j.matdes.2016.05.041.

[57] Shakil SI, Hadadzadeh A, Shalchi Amirkhiz B, Pirgazi H, Mohammadi M, Haghshenas M. Additive manufactured versus cast AlSi10Mg alloy: microstructure and micromechanics. Results in Materials 2021;10. https://doi.org/10.1016/j.rinma.2021.100178.

[58] Ghio E, Cerri E. Additive manufacturing of AlSi10Mg and Ti6Al4V lightweight alloys via laser powder bed fusion: a review of heat treatments effects. Materials 2022;15. https://doi.org/10.3390/ma15062047.

[59] Samuel SC, Arivarasu M, Prabhu TR. High temperature dry sliding wear behaviour of laser powder bed fused Inconel 718. Addit Manuf 2020;34:101279. https://doi.org/10.1016/j.addma.2020.101279.

[60] Karimi J, Antonov M, Kollo L, Prashanth KG. Role of laser remelting and heat treatment in mechanical and tribological properties of selective laser melted Ti6Al4V alloy. J Alloys Compd 2022;897:163207. https://doi.org/10.1016/j.jallcom.2021.163207.

[61] Delahaye J, Tchuindjang JT, Lecomte-Beckers J, Rigo O, Habraken AM, Mertens A. Influence of Si precipitates on fracture mechanisms of AlSi10Mg parts processed by Selective Laser Melting. Acta Mater 2019;175:160–70. https://doi.org/10.1016/j.actamat.2019.06.013.

[62] Javidani M, Arreguin-Zavala J, Danovitch J, Tian Y, Brochu M. Additive manufacturing of AlSi10Mg alloy using direct energy deposition: microstructure and hardness characterization. J Therm Spray Technol 2017;26:587–97. https://doi.org/10.1007/s11666-016-0495-4.

[63] Zhou L, Mehta A, Schulz E, McWilliams B, Cho K, Sohn Y. Microstructure, precipitates and hardness of selectively laser melted AlSi10Mg alloy before and after heat treatment. Mater Char 2018;143:5–17. https://doi.org/10.1016/j.matchar.2018.04.022.

[64] Santos Macías JG, Douillard T, Zhao L, Maire E, Pyka G, Simar A. Influence on microstructure, strength and ductility of build platform temperature during laser powder bed fusion of AlSi10Mg. Acta Mater 2020;201:231–43. https://doi.org/10.1016/j.actamat.2020.10.001.

[65] Wang T, Dai S, Liao H, Zhu H. Pores and the formation mechanisms of SLMed AlSi10Mg. Rapid Prototyp J 2020;26:1657–64. https://doi.org/10.1108/RPJ-02-2020-0036.

[66] Qin H, Xu R, Lan P, Wang J, Lu W. Wear performance of metal materials fabricated by powder bed fusion: a literature review. Metals 2020;10. https://doi.org/10.3390/met10030304.

[67] Ye C, Zhang C, Zhao J, Dong Y. Effects of post-processing on the surface finish, porosity, residual stresses, and fatigue performance of additive manufactured metals: a review. J Mater Eng Perform 2021;30:6407–25. https://doi.org/10.1007/s11665-021-06021-7.

[68] DebRoy T, Wei HL, Zuback JS, Mukherjee T, Elmer JW, Milewski JO, et al. Additive manufacturing of metallic components – process, structure and properties. Prog Mater Sci 2018;92:112–224. https://doi.org/10.1016/j.pmatsci.2017.10.001.

[69] Rosenthal I, Shneck R, Stern A. Heat treatment effect on the mechanical properties and fracture mechanism in AlSi10Mg fabricated by additive manufacturing selective laser melting process. Mater Sci Eng, A 2018;729:310–22. https://doi.org/10.1016/j.msea.2018.05.074.

[70] Gu X, Zhang J, Fan X, Dai N, Xiao Y, Zhang LC. Abnormal corrosion behavior of selective laser melted AlSi10Mg alloy induced by heat treatment at 300 °C. J Alloys Compd 2019;803:314–24. https://doi.org/10.1016/j.jallcom.2019.06.274.

[71] Girelli L, Tocci M, Gelfi M, Pola A. Study of heat treatment parameters for additively manufactured AlSi10Mg in comparison with corresponding cast alloy. Mater Sci Eng, A 2019;739:317–28. https://doi.org/10.1016/j.msea.2018.10.026.

[72] Frey M, Wegner J, Neuber N, Reiplinger B, Bochtler B, Adam B, et al. Thermoplastic forming of additively manufactured Zr-based bulk metallic glass: a processing route for surface finishing of complex structures. Mater Des 2021;198. https://doi.org/10.1016/j.matdes.2020.109368.

[73] Golewski GL. Concrete composites based on quaternary blended cements with a reduced width of initial microcracks. Appl Sci 2023;13. https://doi.org/10.3390/app13127338.

[74] Golewski GL. Mechanical properties and brittleness of concrete made by combined fly ash, silica fume and nanosilica with ordinary Portland cement. AIMS Mater Sci 2023;10:390–404. https://doi.org/10.3934/matersci.2023021.

[75] Golewski GL. The phenomenon of cracking in cement concretes and reinforced concrete structures: the mechanism of cracks formation, causes of their initiation, types and places of occurrence, and methods of detection—a review. Buildings 2023;13. https://doi.org/10.3390/buildings13030765.

[76] Govind V, Praveen KK, Vignesh Rv V, Vishnu A, Vishnu J, Manivasagam G, et al. Fretting wear behavior of Al-Si-Mg-Ni hypoeutectic alloy with varying solutionizing time. Silicon 2023:4193–206. https://doi.org/10.1007/s12633-023-02342-5.

[77] Li J, Lu YH. Effects of displacement amplitude on fretting wear behaviors and mechanism of Inconel 600 alloy. Wear 2013;304:223–30. https://doi.org/10.1016/j.wear.2013.04.027.

[78] Fouvry S, Duó P, Perruchaut P. A quantitative approach of Ti-6Al-4V fretting damage: friction, wear and crack nucleation. Wear 2004;257:916–29. https://doi.org/10.1016/j.wear.2004.05.011.

[79] Golewski GL. Study of strength and microstructure of a new sustainable concrete incorporating pozzolanic materials. Struct Eng Mech 2023;86(4):431–41. https://doi.org/10.12989/sem.2023.86.4.431.